

## Shear velocity structure and azimuthal anisotropy beneath eastern North America from Rayleigh wave inversion

Aibing Li,<sup>1</sup> Donald W. Forsyth, and Karen M. Fischer

Department of Geological Sciences, Brown University, Providence, Rhode Island, USA

Received 21 October 2002; revised 14 March 2003; accepted 2 April 2003; published 2 August 2003.

[1] We have obtained shear velocity structure beneath the northeastern United States and southeastern Canada using Rayleigh wave phases and amplitudes. Thin crust (36–42 km) is observed along the Atlantic coast and in the eastern Appalachian orogen, and thick crust (42–46 km) is imaged in the western Appalachians and in the western New York portion of the Grenville Province. The variation of crustal thickness correlates well with the observed Bouguer gravity anomalies. In the upper mantle, the high-velocity continental keel of cratonic North America is present in the western part of the study area, while a broad low-velocity region is imaged in New England from the Hudson River valley to the White Mountains. This low-velocity anomaly is probably the consequence of past heating of the lithospheric mantle associated with the Montereian hotspot and may represent intrusion of asthenosphere into the edge of the keel. In addition to lateral variations in velocity, we estimate the azimuthal dependence of phase velocity. Strong and relatively uniform shear wave splitting is observed in the study region, but at periods of 100 s or less, the average azimuthal anisotropy of Rayleigh waves is less than 1% and is not significantly different from zero at any individual period. This small degree of azimuthal anisotropy is not consistent with a substantial contribution to shear wave splitting from fossil anisotropy in the lithosphere. Much of the source of the shear wave splitting must lie deeper than 200 km. *INDEX TERMS:* 7218 Seismology: Lithosphere and upper mantle; 7255 Seismology: Surface waves and free oscillations; 8180 Tectonophysics: Tomography; 9350 Information Related to Geographic Region: North America; *KEYWORDS:* Rayleigh wave, shear velocity, anisotropy, North America

**Citation:** Li, A., D. W. Forsyth, and K. M. Fischer, Shear velocity structure and azimuthal anisotropy beneath eastern North America from Rayleigh wave inversion, *J. Geophys. Res.*, 108(B8), 2362, doi:10.1029/2002JB002259, 2003.

### 1. Introduction

[2] We have chosen to study the seismic velocity structure of the northeastern United States and southeastern Canada (Figure 1), because it includes a major transition in lithospheric thickness, a well-documented pattern of shear wave splitting indicating seismic anisotropy, and a distribution of broadband seismic stations sufficient to allow detailed, 3-D mapping of the velocity structure using surface wave tomography. In addition, the distribution of stations makes it possible to measure azimuthal variations in Rayleigh wave velocity that offer the potential of estimating the depth extent of the anisotropic region giving rise to shear wave splitting. Asthenospheric flow can be deflected around and beneath thick continental lithosphere, perhaps inducing detectable variations in seismic anisotropy that would constrain the pattern of flow. In addition, anisotropy

within the lithosphere may record mantle fabric created by past episodes of deformation.

[3] Our area of interest contains several different lithospheric provinces: the Grenville Province, the Appalachian Orogen, and the western edge of the Atlantic passive margin [Rankin, 1994]. It manifests a rich variation in surface geology with crustal rocks dating from the Proterozoic Grenvillian orogeny (1.1 Ga), the Phanerozoic Appalachian orogeny, Triassic and Jurassic rifting, and Cretaceous plutonism in the Montereian Hills and New England [Hatcher, 1989; Hoffman, 1989; Rankin, 1994].

[4] Crustal structure in the area has been constrained by numerous seismic studies. Summaries of seismic refraction and reflection profiles in North America indicate that the crust varies from 40–45 km in the Grenville province to 30–35 km at the Atlantic coast, with some suggestion of crustal thickening beneath the Appalachians [Braile *et al.*, 1989; Mooney and Braile, 1989; Taylor, 1989]. Using receiver functions at the stations of the linear Missouri to Massachusetts Broadband Seismometer Experiment (MOMA), Li *et al.* [2002a] found that the crust reaches its maximum thickness beneath the western Appalachians in Pennsylvania, with thinner crust both in the eastern Appalachians of southern New York and New England and in the Grenville

<sup>1</sup>Now at Department of Geosciences, University of Houston, Houston, Texas, USA.

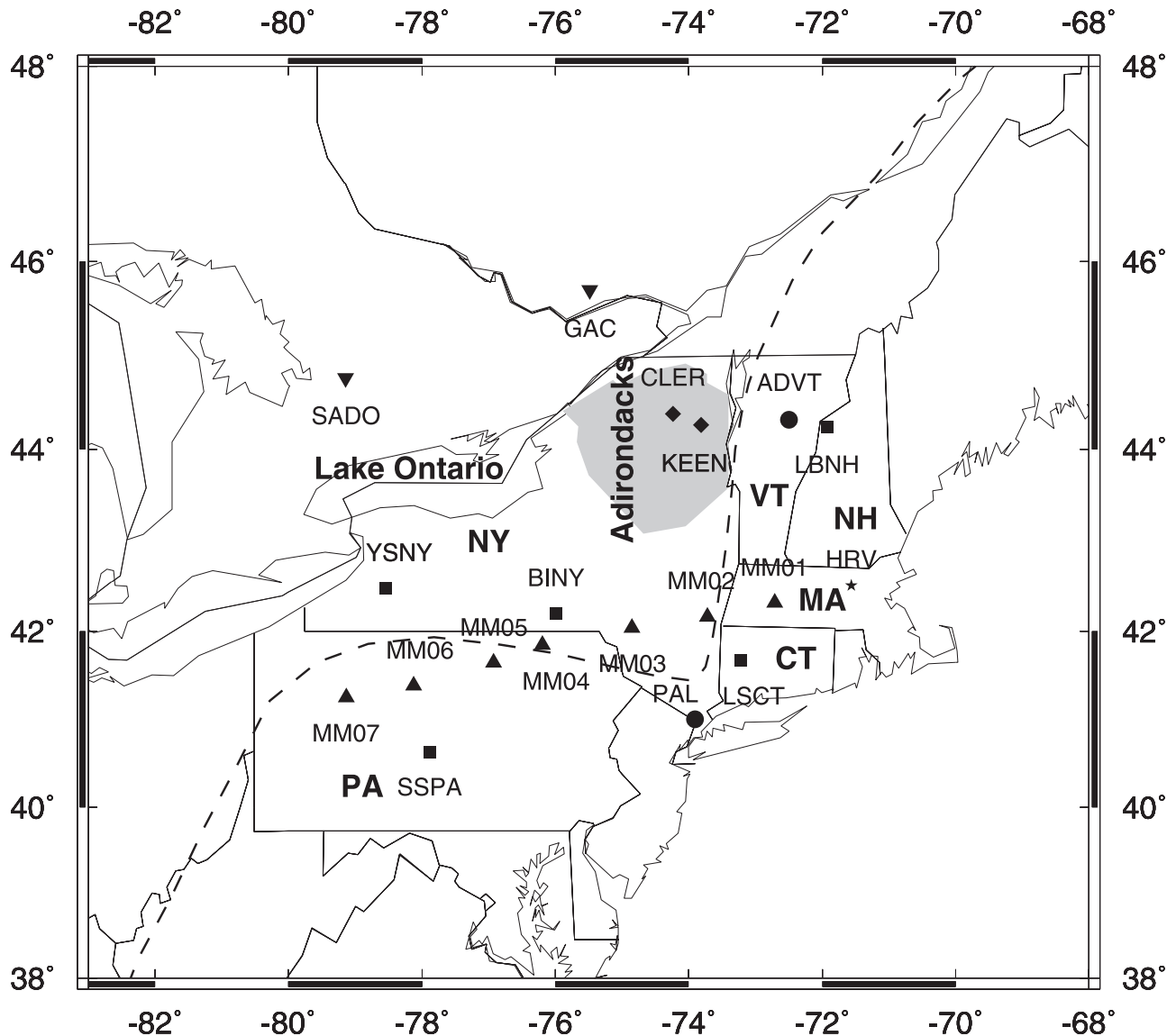


**Figure 1.** Map of the study area and seismic stations. Different symbols indicate stations from different seismic experiments. Triangles are for the MOMA stations, squares are for the USNSN stations, stars are for the IRIS GSN stations, inverse triangles are for the CNSN stations, diamonds are for the ABBA stations, and circles are for stations from the New England Broadband Experiment. Station name is plotted near the station. Shaded region is the Adirondack Mountains. Dashed line delineates the Appalachian front.

Province to the west. Crustal  $P$  wave velocity ( $V_p$ ) in the Grenville province is in general greater than that in the Appalachians and both  $V_p$  and  $V_p/V_s$  are very high in the middle and upper crust beneath the Adirondack Mountain region of the Grenville Province [Hughes and Luetgert, 1991, 1992; Levin et al., 1995; Musacchio et al., 1997; Zhu and Ebel, 1994].

[5] Seismic tomography studies have imaged the eastern edge of the fast shear velocity North American continental keel [Grand, 1994; Grand et al., 1997; Van der Lee and Nolet, 1997; Larson and Ekstrom, 2001]. Whereas Van der Lee and Nolet found a broad indentation in the keel edge centered on New York, the eastern keel margins imaged by Grand, and Larson and Ekstrom are considerably smoother.

Body wave tomography [Rondenay et al., 2000] revealed a narrow NW-SE trending low-velocity zone in the upper mantle of the Grenville province of the Canadian Shield, but although this feature overlaps part of the low-velocity indentation of Van der Lee and Nolet, it is much more localized. Levin et al. [2000] found a narrower low  $S$  wave velocity corridor within the slow region imaged by Van der Lee and Nolet, and recently, measuring Rayleigh wave phase velocities versus azimuth at several local areas in northeastern United States, Menke and Levin [2002] suggested that this anomaly is in fact a low-velocity layer that deepens seaward. The discrepancy between different models leads to ambiguity about important issues, such as the morphology of the keel edge and the shape and origin of

the low-velocity anomaly. A more detailed investigation of Rayleigh wave propagation in this area should resolve some of these issues.

[6] Shear wave splitting measurements indicate that azimuthal anisotropy exists beneath eastern North America and varies three dimensionally [Vinnik *et al.*, 1992; Silver, 1996; Barruol *et al.*, 1997; Levin *et al.*, 1999; Fouch *et al.*, 2000; Rondenay *et al.*, 2000]. However, whether the anisotropy is dominated by frozen fabric in the lithosphere and/or lattice-preferred orientation induced from sublithospheric flow is still an open question [Vinnik *et al.*, 1992; Silver, 1996]. For example, in eastern North America, Silver argued that the anisotropy is located in the lithosphere based on the consistency between fast directions of shear wave splitting and geological trends. On the other hand, Vinnik *et al.* preferred an asthenospheric origin for the anisotropy. Fouch *et al.* used mantle flow models with indented keel morphology of the craton to predict SKS splitting from the asthenosphere, and concluded that the presence of anisotropy in both the lithosphere and asthenosphere was likely. Levin *et al.* proposed a model of two-layer anisotropy in the Appalachians based on analyzing the back-azimuthal variation of fast directions from shear wave splitting analysis. Shear wave splitting analysis lacks constraints on the vertical distribution of anisotropy because it is usually obtained from teleseismic core converted phases, such as SKS, PKS, and SKKS, which sample anisotropy from the core-mantle boundary to the surface. Surface waves at different periods are sensitive to velocity structure at different depth ranges and therefore have great potential to resolve depth variations of anisotropy.

[7] In this paper, we map the 3-D and anisotropic variations in seismic velocity in northeastern United States and southeastern Canada with a much higher density of Rayleigh wave paths than has been employed in previous studies. In addition, by employing a method [Forsyth and Li, 2003] that accounts for complexity in the incoming wave fields, we are able to determine the phase velocities more precisely and to extend the analysis to shorter periods than is typical of studies with teleseismic sources, yielding better resolution of lithospheric and asthenospheric structure. We discuss resolution of the velocity variations, including the trade-off between lateral heterogeneity and azimuthal anisotropy.

## 2. Data Collection and Analysis

[8] We used fundamental mode Rayleigh waves recorded at 19 broadband seismic stations located in northeastern United States and southeastern Canada (Figure 1). The stations are from six different networks and portable broadband experiments that were in operation from February 1995 to March 1996. There are seven stations (MM01 to MM07) from the MOMA array [Fischer *et al.*, 1996], five stations (BINY, LBNH, LSCT, SSPA, and YSNY) from the United States National Seismic Network (USNSN), one station (HRV) from the IRIS Global Seismic Network, two stations (GAC and SADO) from the Canadian National Seismic Network (CNSN), two (ADVT and PAL) from the New England Broadband Experiment [Levin *et al.*, 1996], and two (CLER and KEEN) from the Adirondack Broad

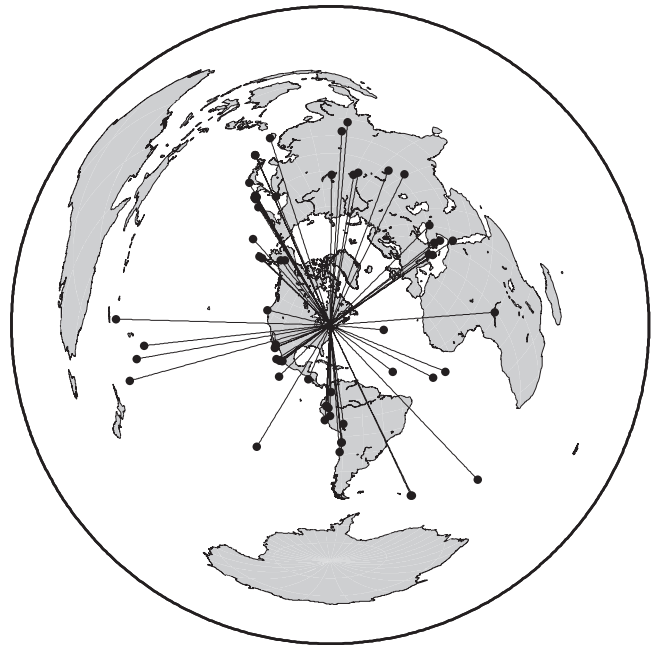


**Figure 2.** Locations of earthquakes used as Rayleigh wave sources in this study. The plot is centered on the middle of the array from azimuthal equidistant projection.

Band Array (ABBA) (S. Roecker, personal communication, 2000).

[9] We used earthquakes in a distance range of  $30^{\circ}$ – $120^{\circ}$  with body wave magnitude larger than 5.5. Of the more than 200 potential events, only 64 provided high-quality data for our analysis. The distribution of these events (Figure 2) shows a good azimuthal coverage, which is important for resolving both lateral heterogeneity and azimuthal anisotropy. There are denser crossing ray paths within the array marked by the open box in Figure 3, where the resolution is expected to be higher than in the surrounding area.

[10] In order to select fundamental mode Rayleigh waves with high signal-to-noise ratio and reasonable coherence from station to station, we normalized station instrument responses to that of a CMG-3T and applied different band-pass filters with center frequencies ranging from 8 to 50 mHz to the vertical component seismograms. Each filter was a 10-mHz-wide, fourth order, double-pass Butterworth filter. In each passband, only those Rayleigh waves with good signal-to-noise ratio were retained and then isolated with a rectangular window with cosine tapers on the ends. Window length was determined by the epicentral distance and dispersion characteristics, but the same window length was used for all seismograms for a given event. Most data at short periods (less than 33 s) display strong interference due to multipathing or scattering and show inconsistency between stations, reflecting a complicated incoming wave field. Shorter paths that cross fewer tectonic boundaries tend to have cleaner records indicating that scattering is the dominant source of the complexity, but some events have spectral holes due to the excitation function at the source. Passbands near these spectral holes typically would be eliminated at this stage, or, if retained, be poorly fit in the inversion process described below and therefore given little weight in the final analysis. Fundamental mode Rayleigh

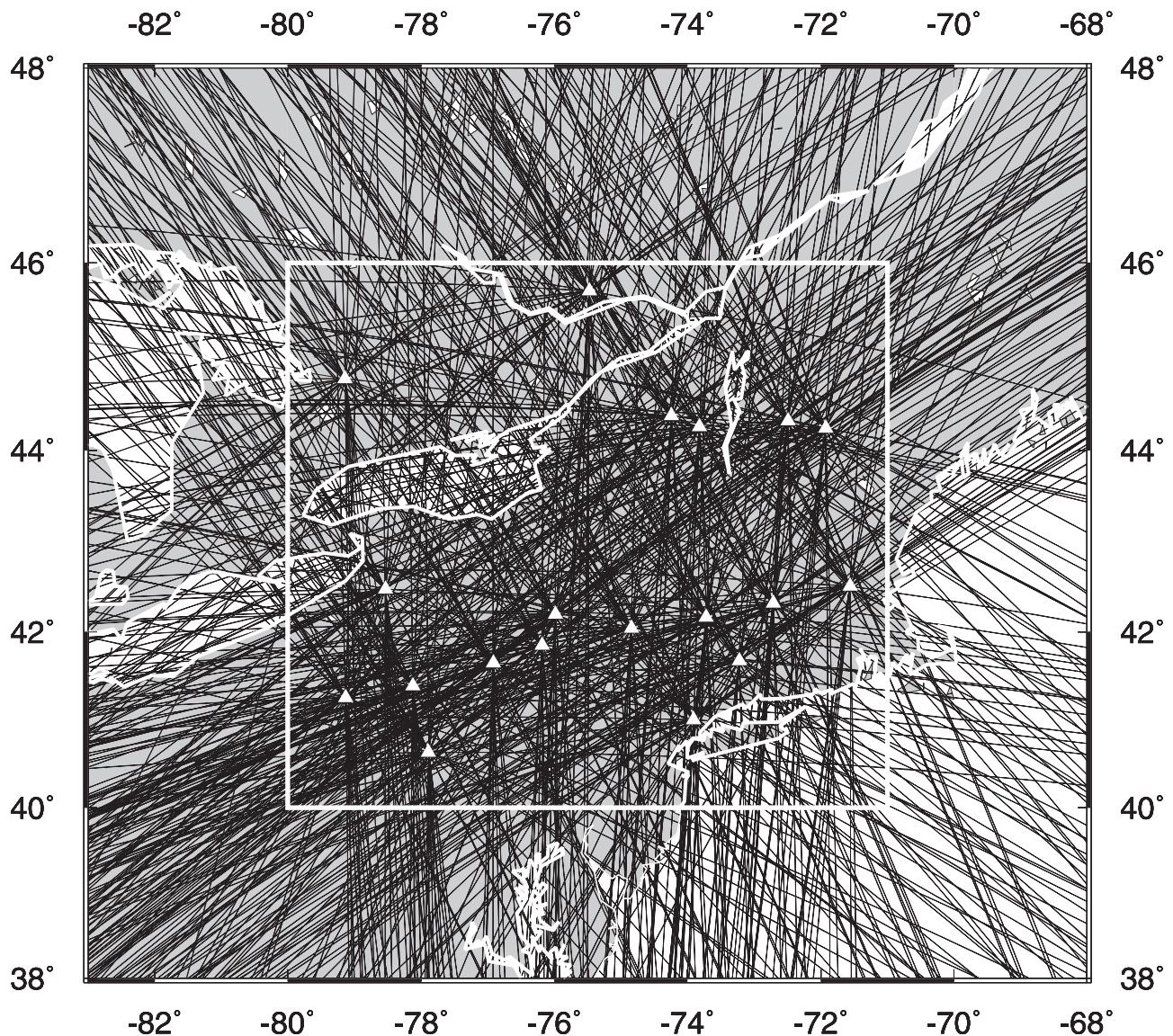


**Figure 3.** Great circle paths in the vicinity of the array at periods of 50 s. Open triangles represent stations. Dense crossing of ray paths exists in the area marked by the open box, where high resolution is expected.

waves also become simpler and cleaner at longer periods, but the signal-to-noise ratios decrease due to reduced amplitudes and poor long-period response at some stations. Frequency bands from individual events with incoherent scattering or signal-to-noise ratios less than about three were rejected, leading to more data and better resolution in the 30–80 s range than at shorter or longer periods.

[11] Rayleigh wave phase and amplitude were measured using a positive Fourier transform of the filtered and windowed seismograms. Amplitudes were also corrected for geometric spreading, anelastic attenuation, and station site effects using the expression  $A_i = A_i^0 e^{-\gamma(\Delta_i - \Delta_0)} (\sin(\Delta_i \pi / 180))^{1/2} / c_i$ , where  $A_i^0$  is the amplitude at station  $i$  before the correction, and  $\gamma$  is the attenuation coefficient at a given frequency. The  $\gamma$  values used in eastern North America are from Mitchell [1995]. The  $\Delta_i$  and  $\Delta_0$  are epicentral distances to station  $i$  and the reference station, respectively, and  $c_i$  is a constant value for the site effect or

station response at each station, which was solved for in the inversion.

### 3. Phase Velocity Inversion

#### 3.1. Methodology

[12] We adopted a two-step inversion of Rayleigh wave data for velocity structure. The first step was to image phase velocities by inverting Rayleigh wave amplitude and phase data, and the second step was to obtain velocity structure from phase velocities. In this section, we only describe the inversion for phase velocities.

[13] Rayleigh waves at a seismic array are affected by velocity structure everywhere along the ray path from source to receiver, and an important question is how to separate the effects of structure outside the seismic array from those of the structure beneath it. In traditional surface wave tomography, great circle ray paths are assumed [e.g.,

Montagner, 1985]. However, surface waves may deviate from great circle paths due to lateral heterogeneities, resulting in changes in direction of propagation across an array, focusing or defocusing of energy, multipathing, and incoherent scattering [Capon, 1971; Alsina et al., 1993; Friederich et al., 1994]. Traditional array processing techniques assume planar wave fronts, solving for the apparent direction of approach in addition to phase velocity. The effects of nonplane wave energy on phase velocity are taken into account in recently developed methods [Friederich and Wielandt, 1995; Forsyth et al., 1998; Forsyth and Li, 2003; Li et al., 2002b, 2003].

[14] In this paper, we adopted the two-plane-wave inversion technique [Forsyth and Li, 2003] to simultaneously solve for the incoming wave field and phase velocity. The wave field is represented by the sum of two plane waves with initially unknown amplitude, phase, and propagation direction, a total of six parameters to describe the incoming wave field at each frequency. Although the two-plane-wave assumption is a simple approximation of a potentially complex interference pattern, in many cases it provides a good description of the spatial pattern of amplitude variations across the array. The advantage of this method is that it uses a minimum number of model parameters to account for the nonplanar energy in the incoming wavefield. We excluded those data whose incoming wave fields are too complicated to be represented by two plane waves, usually at short periods with ray paths traveling through different tectonic regions (ocean and continent). The simulated annealing method [Press et al., 1992] is used to solve for initial plane wave parameters before inverting for phase velocities. Then a generalized linear inversion is employed to solve for both phase velocities on a grid of nodes and adjusted plane wave parameters for each event. Both of these steps are repeated in each iteration toward a solution. Once a solution is found, the apparent standard deviation for each event in each frequency band is found. The observations are then weighted in inverse proportion to these standard deviations and the inversion repeated, so that observations with relatively poor signal-to-noise ratio or interference patterns that are poorly described by the two-plane-wave approximation are given little weight.

[15] Surface wave phase and group velocity in a slightly anisotropic media [Smith and Dahlen, 1973] can be expressed as

$$c(\omega, \psi) = B_0(\omega) + B_1(\omega) \cos(2\psi) + B_2(\omega) \sin(2\psi) + B_3(\omega) \cos(4\psi) + B_4(\omega) \sin(4\psi), \quad (1)$$

where  $c(\omega, \psi)$  is Rayleigh wave phase velocity,  $\omega$  is frequency, and  $\psi$  is back azimuth. We ignored the  $4\psi$  terms because they are difficult to constrain and are expected to be small for Rayleigh waves. To describe the variations of phase velocity across the array, we use a continuous function that is a weighted average of velocities at neighboring grid points. The grid in the study area is shown in Figure 4. There are a total of 289 grid nodes that are distributed unevenly in the region. The density of grid nodes is higher in the center of the region with a spacing of  $0.75^\circ$  in longitude and  $0.5^\circ$  in latitude, and the density is

lower along edges with nodes at  $1.5^\circ$  by  $1^\circ$ . It is important to have grid points in an area larger than where phase velocities are well resolved by crossing ray paths, because phase velocities at these outer points can absorb some of the phase effects of more complex wave fields that are not completely represented by two plane waves.

[16] The number of plane wave parameters for the incoming wave fields is  $6N$ , where  $N$  is the number of events. The number of model parameters for phase velocity varies in different cases. It is 1 for a uniform isotropic velocity and  $3M$  when allowing  $B_0$ ,  $B_1$ , and  $B_2$  to vary at each grid node, where  $M$  is the number of the nodes. Other cases include 2-D variation of isotropic phase velocity only, with uniform anisotropic terms over the whole area or in different subregions. Each seismogram provides two pieces of information for a given frequency, i.e., phase and amplitude, or real and imaginary components as we employ in the tomographic inversion.

[17] To solve for phase velocities and the incoming wave fields simultaneously, we use a standard, iterative, linearized inversion technique [Tarantola and Valette, 1982]. Letting  $\mathbf{m}_0$  be a starting model, synthetic data are  $\mathbf{d}_0 = \mathbf{g}(\mathbf{m}_0)$ . The solution to the general, nonlinear, least squares inversion is given by

$$\Delta \mathbf{m} = (\mathbf{G}^T \mathbf{C}_{nn}^{-1} \mathbf{G} + \mathbf{C}_{mm}^{-1})^{-1} (\mathbf{G}^T \mathbf{C}_{nn}^{-1} \Delta \mathbf{d} - \mathbf{C}_{mm}^{-1} [\mathbf{m} - \mathbf{m}_0]), \quad (2)$$

where  $\mathbf{m}$  is the current model,  $\Delta \mathbf{m}$  is the change to the current model,  $\Delta \mathbf{d}$  is the difference between the predicted and observed data,  $\mathbf{G}$  is the Frechet derivative of the operator  $\mathbf{g}$ ,  $\mathbf{C}_{nn}$  is the a priori data covariance matrix, and  $\mathbf{C}_{mm}$  is the a priori model covariance matrix. Off-diagonal terms are introduced into  $\mathbf{C}_{mm}$  to smooth the solution [Constable et al., 1987].  $\mathbf{C}_{nn}$  is assumed to have only diagonal terms. We assigned an a priori error of 0.1 to normalized real and imaginary data (maximum amplitudes for each event were normalized to 1.0). An a posteriori standard deviation of the data from each individual earthquake is estimated after 10 iterations and assigned as the new a priori error for a second round of iterations, thus giving less weight to the data which are poorly represented by two plane waves or have lower signal-to-noise ratios. This eliminates the bias in phase velocity from complicated incoming wave fields which cannot be well described by our simple assumption. We increased the model variance by a factor of 10 at the outer points on the grid. These extremely weakly damped nodes can absorb travel time deviations from the idealized two-plane-wave model and protect the interior area of interest from being affected.

## 3.2. Model Resolution

### 3.2.1. Variance Versus Resolution

[18] As in all inverse problems, there is a trade-off between model variance and model resolution. These trade-offs can be described by the a posteriori model covariance matrix  $\mathbf{C}_{MM}$ ,

$$\mathbf{C}_{MM} = (\mathbf{G}^T \mathbf{C}_{nn}^{-1} \mathbf{G} + \mathbf{C}_{mm}^{-1})^{-1},$$

and the model resolution matrix  $\mathbf{R}$ ,

$$\mathbf{R} = (\mathbf{G}^T \mathbf{C}_{nn}^{-1} \mathbf{G} + \mathbf{C}_{mm}^{-1})^{-1} \mathbf{G}^T \mathbf{C}_{nn}^{-1} \mathbf{G}.$$

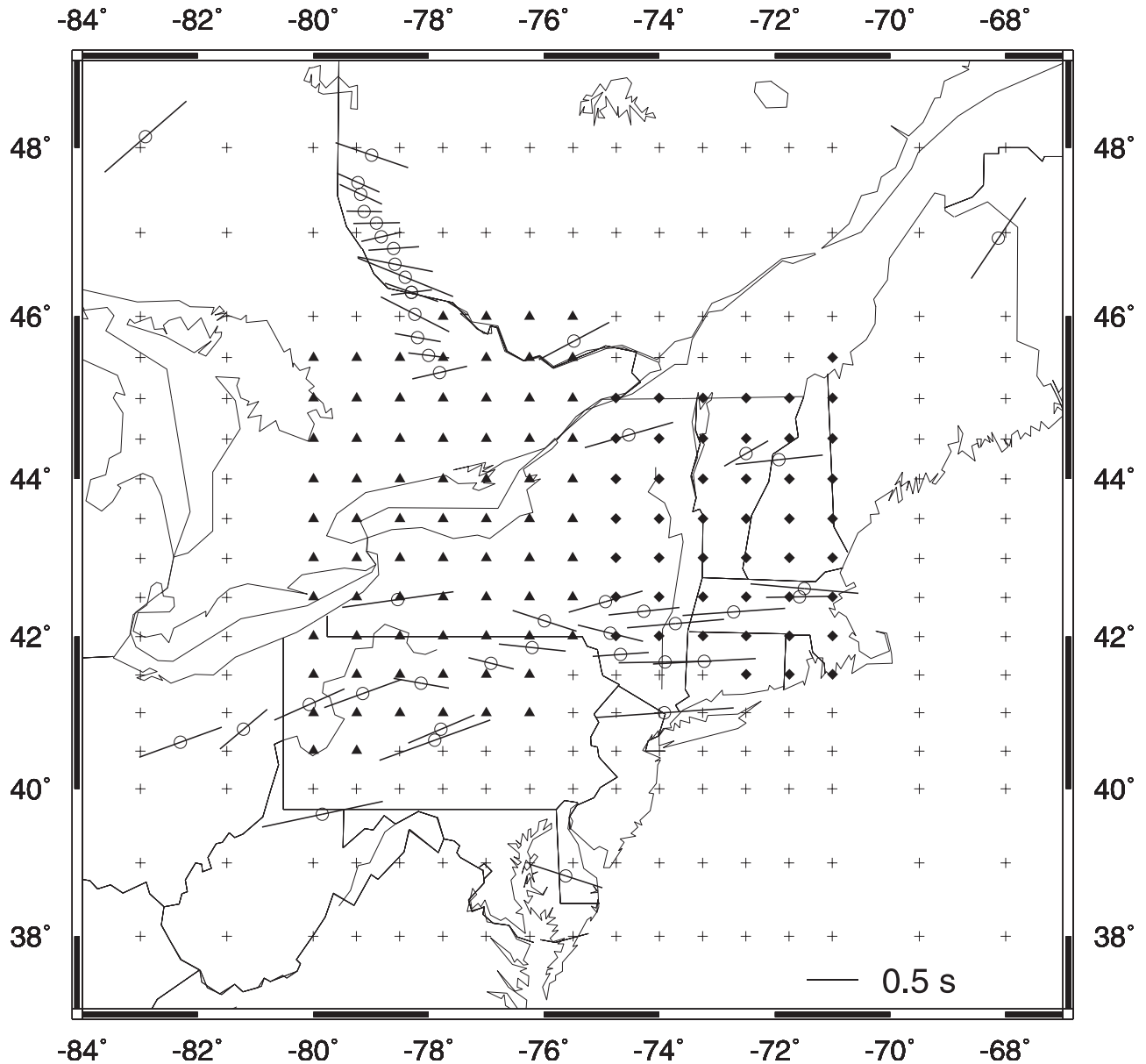


**Figure 4.** Grid nodes used in Rayleigh wave phase velocity inversions. Triangles and diamonds correspond to the high-velocity region and the low-velocity region in Figure 12, respectively. Grouping grid nodes by region is useful for solving lateral variations in anisotropy. Open circles are stations at which shear wave splitting measurements are available from previous studies (for complete references, see *Fouch et al.* [2000]). The strike of solid bar is parallel to shear wave splitting fast direction at a given station and the length of the bar is proportional to splitting time.

Two important parameters in describing model resolution and variance are the rank and the standard error (square root of the variance at a given map point). The rank is the sum of diagonal terms in  $\mathbf{R}$ , which is equivalent to the number of pieces of information extracted from the data for both velocity and wave field parameters. Since we represent phase slowness at every point as a 2-D, Gaussian weighted function of surrounding nodes that has a characteristic scale length  $L_w$ , an appropriate  $L_w$  plays an important role in balancing model variance and resolution. In Table 1, we compare resolution and variance values from three models which were obtained using the same data set, Rayleigh waves at period of 50 s

with different  $L_w$  as 60, 80, and 100 km, respectively. At the shorter-scale length, the rank is higher and the misfit is smaller, but the standard error is larger.  $L_w$  can be determined either based on Fresnel zone width or on the trade-off between resolution and variance, which depends on the density of crossing ray paths and the grid size. In general, denser ray paths and smaller grid cells allow use of a smaller  $L_w$ . The smaller the  $L_w$ , the higher the resolution (smaller-scale variations on phase velocities can be resolved) and the larger the variance. If  $L_w$  is too small, phase velocities show strong lateral oscillations. On the other hand, if  $L_w$  is too big, we obtain a very smoothed solution with small variance but little resolution

**Table 1.** Ranks and Standard Errors for Velocity Models With Different Smoothing Lengths

Smoothing Length, km	Total Rank	Rank for Velocity	Standard error, m/s at $-76^\circ$ , $42^\circ$
100	342.6	59.9	15.14
80	358.4	76.9	19.56
60	378.0	100.5	27.24

of lateral variations in phase velocity. We chose  $L_w$  equal to 80 km in this study after testing several different values.

### 3.2.2. One-Plane Wave Versus Two-Plane Wave

[19] Although observations and theoretical analysis [Capon, 1971; Alsina et al., 1993; Friederich et al., 1994] have shown that nonplane wave energy is present in the incoming wave field of surface waves, does the two-plane-wave assumption used in this study indeed do a better job than the one-plane-wave assumption in tomographic inversions? To address this question, we conducted the same inversion for phase velocities as described above except representing each incoming wave field as one plane wave. Figure 5 shows the comparison of the results from the one-plane-wave and two-plane-wave assumption at a period of 50 s. Compared with a one-plane-wave inversion, introducing the two-plane-wave representation clearly improves the fit to amplitude and also reduces the variance in phase by about 30%. In addition, the rank for phase velocities under the two-plane-wave assumption is 77, higher than 64 from the one-plane-wave assumption, indicating that modeling the interference improves the resolution of horizontal variations in phase velocity. The increase in the rank for velocity parameters, not for the total model parameters, will result only if the improvement in the model with the two-plane-wave parameters is significant. An  $F$  test shows that the probability is less than 1% that the reduction in variance could have arisen by chance from the addition of  $6N$  random parameters. In other words, the improvement in the model from the one-plane-wave to the two-plane-wave method is significant at the 99% confidence level. Therefore the two-plane-wave assumption, although simple, does efficiently account for nonplane wave energy in the incoming wave field and increases the resolution for phase velocities.

### 3.2.3. Synthetic Modeling

[20] We conducted resolution tests using synthetic data calculated from given phase velocity models. Synthetic Rayleigh wave data share the same event information as the real data, and the synthetic incoming wave field for each event is assumed as the sum of two plane waves with known initial amplitude, phase, and propagation direction. The choice for the two plane waves is arbitrary. In our modeling, one plane wave propagates at  $4^\circ$  from the great circle path with an initial amplitude of 0.7 and the other travels at  $-10^\circ$  off the great circle path with an amplitude of 0.3, which are typical observed directions and normalized amplitudes. Both plane waves have initial phases of zero. Gaussian noise is added to predicted amplitudes and phases. A Gaussian distribution from 0 to 1 is generated for amplitudes using the standard deviation and mean value

obtained from the inversions of real data and a random distribution from 0 to  $2\pi$  is added to the phases. The noise in the amplitudes and phases is converted to real and imaginary parts and added to the predicted values. Then the synthetic amplitude and phase data are inverted by applying the two-plane-wave technique used for the original data.

[21] Two checkerboard tests with wavelengths of roughly 150 and 400 km are shown in Figure 6. A smoothing length of 80 km is used in the inversions and in generating the maps as was applied in analysis of the real data. The input checkerboards alternate fast and slow anomalies of  $\pm 3\%$ . However, only 2% anomalies are shown in Figure 6a for the model of 150 km wavelength, which is due to the relatively large smoothing length used in constructing the map. The pattern of the small-scale anomalies can be largely recovered at 50 s (Figure 6b) and the resolution is clearly higher at places where more stations are distributed such as along the MOMA array (Figure 1). The strength of the anomalies is reduced in the recovered models. However, the anomalies with a wavelength of 150 km cannot be resolved at 100 s; they are smeared together or averaged out in the solution (Figure 6c). The checkerboard model with a 400-km wavelength is well retrieved at both 50 and 100 s (Figures 6e and 6f). Smearing is found at the outside corners of the maps. Anomalies at some places in the solution (Figure 6e) are stronger than in the input models (Figure 6d) due to the tendency of the minimum length model criterion to concentrate anomalies in the areas that are most sensitive to changes in model parameters, i.e., best constrained. On average, however, the amplitudes of anomalies in well-constrained regions are similar to those of the input model. This synthetic modeling demonstrates the resolving power of our method and data. Our lateral resolution is  $\sim 150$  km at short periods and 300–400 km at longer periods, indicating that the resolution decreases with increasing depth for 3-D structure.

## 3.3. Isotropic Phase Velocities

### 3.3.1. Average Phase Velocity

[22] Since our area of interest contains several distinctive structures, the North American craton, the Appalachian orogenic belt, and the margin of North America and the Atlantic, a reasonable 1-D phase velocity model in the area should be obtained first before solving for lateral variations of phase velocities. Results from an inversion for average phase velocities in the study area are shown in Figure 7. The phase velocities increase with period from 3.614 km/s at 20 s to 4.211 km/s at 125 s. Because only one phase velocity model parameter needs to be obtained per period in this inversion, these values are all well constrained with standard deviation from 0.004 to 0.007 km/s. These phase velocities are generally smaller than those typically found in shield regions [Knopoff, 1972] at periods longer than 50 s. The lower velocities are probably due to a strong low-velocity zone beneath New England and the Atlantic coast [Van der Lee and Nolet, 1997]. These average phase velocities were used as starting values in the inversions for 2-D variations of phase velocities.

### 3.3.2. Phase Velocity Maps

[23] Using the average phase velocities obtained above as starting values, we inverted for isotropic phase velocities at

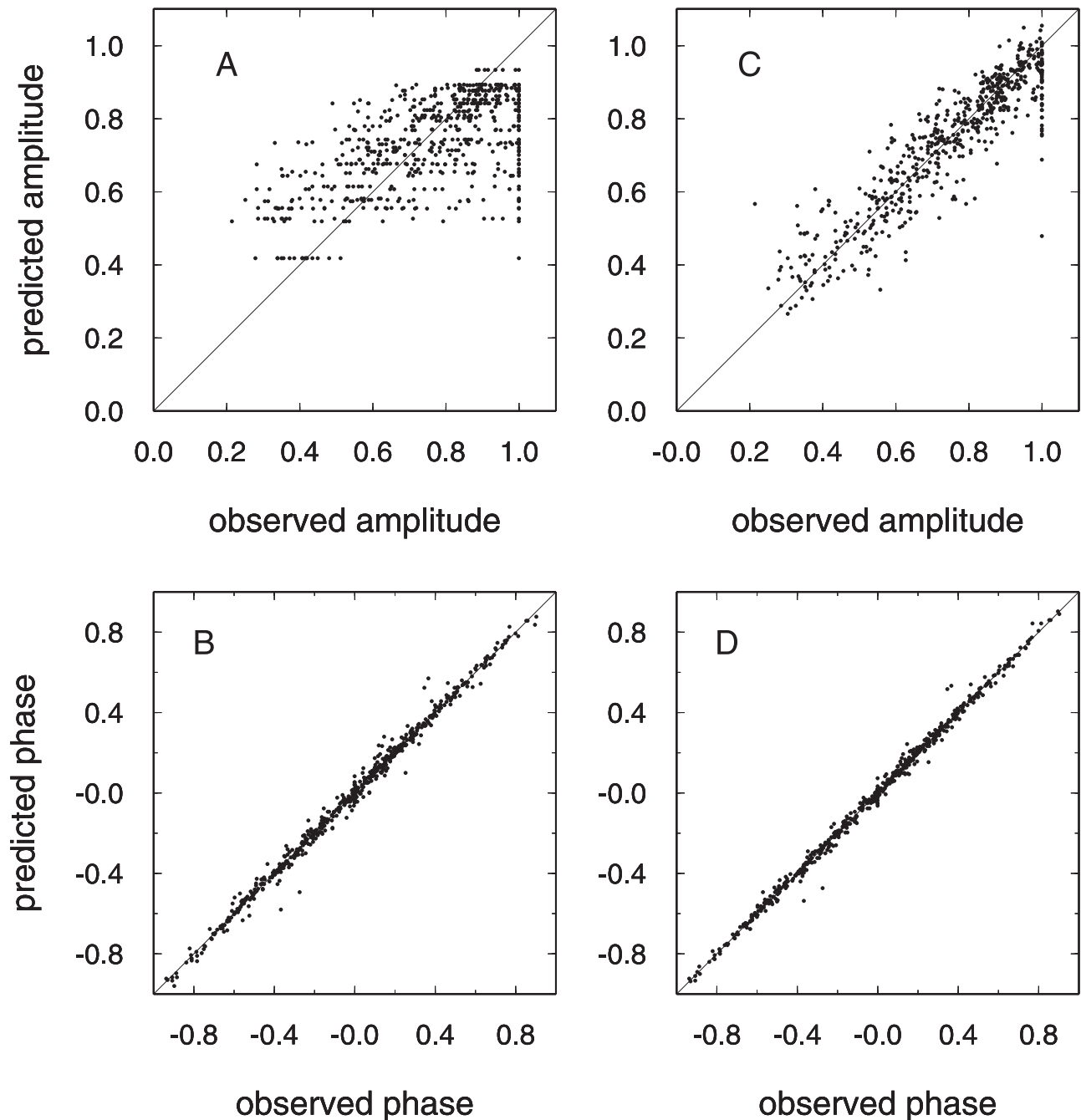


**Figure 5.** Comparison of predicted and observed (top) Rayleigh wave amplitudes and (bottom) phases at 50 s. (a, b) Inversion in which the incoming wave field is represented as one-plane wave and (c, d) Inversion under the two-plane wave assumption. Note that the predicted data from the inversion with the two-plane wave assumption fit the data much better.

each grid node. An a priori standard deviation of 0.25 km/s is assigned to phase velocity terms to provide light damping. Both minimum length and model smoothing criteria were applied in the inversion. Phase velocity maps at a fine spacing ( $0.1^\circ$  by  $0.1^\circ$ ) were generated by weighted averaging of the values at the grid nodes. The weights were calculated with a Gaussian weighting function of the distance between a map point to each grid node with the characteristic length of 80 km, which is the same as we used in the inversion. This step is important because a large

trade-off exists between adjacent grid nodes, and the average of phase velocity in an area is better constrained than each individual grid value. As long as the averaging length in this step is the same as in the inversion, the resulting phase velocity map is identical to the velocities used to predict the travel times, i.e., those used to match the observed phases. The standard errors of phase velocity measurements can be estimated based on the model covariance matrix and the weighting function. One example is given in Figure 8h showing twice the standard errors in

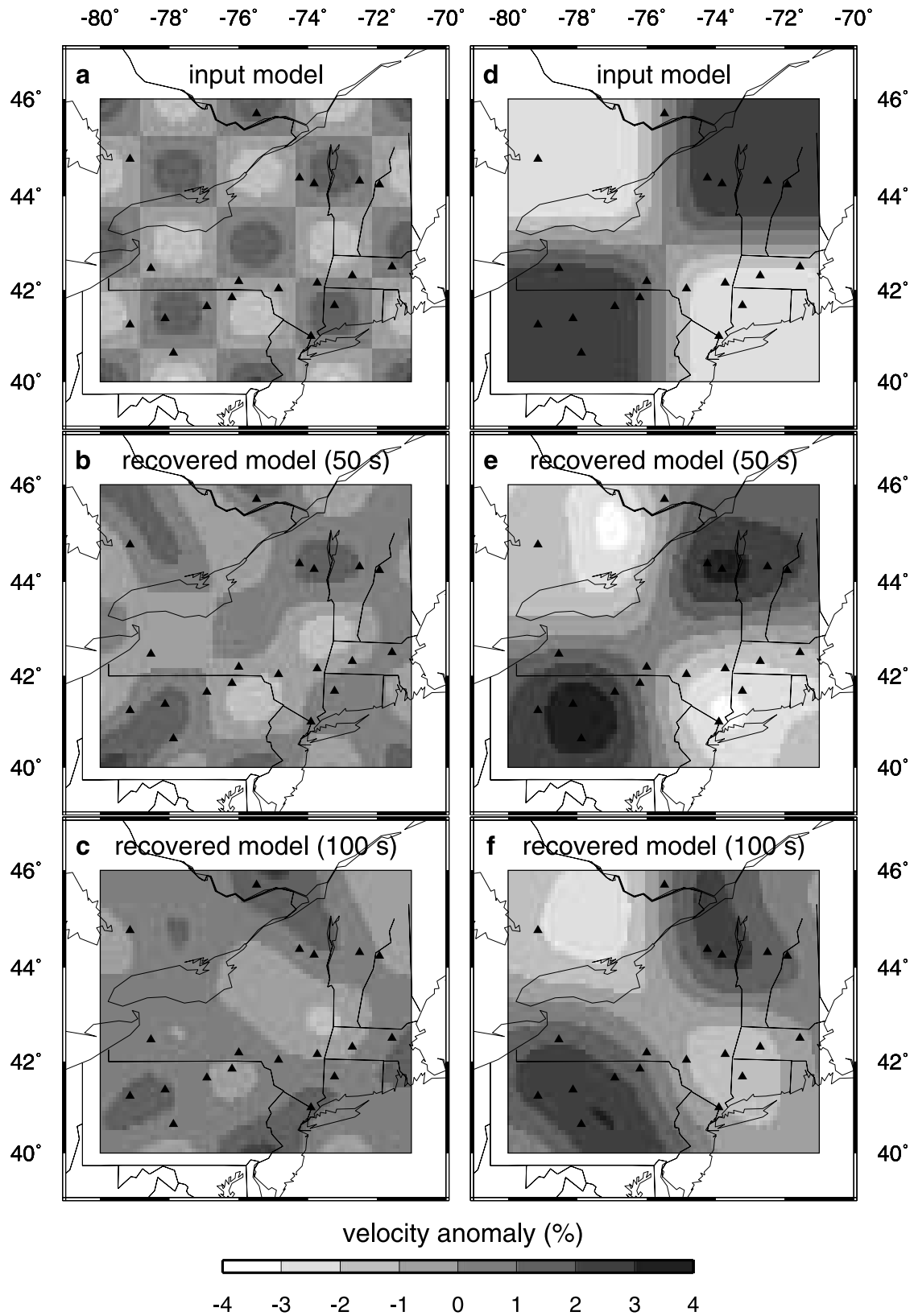


**Figure 6.** Resolution test for Rayleigh wave phase velocity inversions. (a, d) Two input models. (b, e, c, f) Corresponding recovered models at periods of 50 and 100 s, respectively.

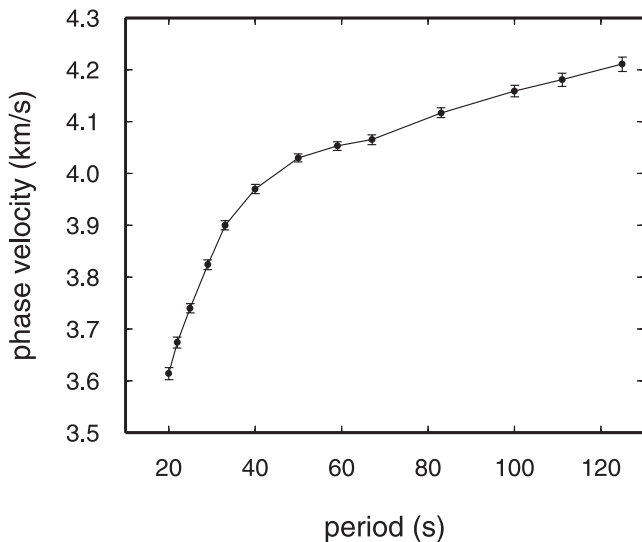


**Figure 7.** Average Rayleigh wave phase velocities at 13 periods ranging from 20 to 125 s. Error bars represent two standard deviations.

percent of phase velocity perturbations at 50 s. Deviations from the starting model exceeding two standard deviations are significant at approximately the 95% confidence level, hence this display allows a quick assessment of the significance of any particular feature in the velocity anomaly map. Although this map is not equivalent to the resolution matrix and the absolute values depend on the smoothing and damping, it does provide an excellent portrayal of the pattern of the resolving power in the data; areas with smaller standard error are better resolved than those with higher standard error. The variance is lower in the interior of the array with the lowest values along the MOMA array where both stations and crossing ray paths are denser, while the resolution at the four corners is poor. The variance of phase velocity itself increases with period because the same magnitude error in Rayleigh wave phase produces larger uncertainties in travel times at longer periods.

[24] The maps of phase velocity anomaly at periods of 20, 25, 33, 50, 67, 100, and 125 s are shown in Figure 8. Each Rayleigh wave phase velocity provides integrated information about velocity structure over a broad depth range with the depth of maximum sensitivity to shear velocity at roughly one third of the wavelength. The 20 and 25 s Rayleigh waves mainly sample crustal structure with greatest sensitivity at depths of 25–30 km. Relatively high velocities are observed near the Adirondacks and along the coast, and a large low-velocity region is imaged at the northern border of Pennsylvania (Figures 8a and 8b). At 33 s, maximum sensitivity to structure occurs at depths around 40 km, including the lower crust and the top of the upper mantle. At this period (Figure 8c), there is a low-velocity band oriented in the NE-SW direction. Strong, fast anomalies are imaged along the Atlantic coast and in the northwest corner. Phase velocities at this period reflect the variation of crustal thickness and velocity perturbations in the crust or uppermost mantle.

[25] Two-dimensional phase velocities at 50 s (Figure 8d), which are most sensitive to a depth of 70 km, image the fast

velocity, North American continental keel in the northwest part of the area and a slow velocity band that correlates well with the Appalachian orogen. The observation of a high-velocity keel agrees with many previous results from seismic tomography [Alsina *et al.*, 1996; Grand *et al.*, 1997; Van der Lee and Nolet, 1997; Larson and Ekstrom, 2001]. Strong, low phase velocity anomalies at 67 s (Figure 8e) are imaged in the eastern part of the area, forming an indentation along the eastern edge of the keel. The intact high-velocity keel in the west disappears at longer periods (Figures 8f and 8g), which roughly agrees with the broad low-velocity zone in the same location observed by Van der Lee and Nolet.

## 4. Shear Wave Velocity Structure

### 4.1. Inversion Method

[26] We inverted phase velocities at each point on the map to obtain 3-D shear wave velocity structure. The data in this inversion are previously resolved phase velocities at 13 periods ranging from 20 to 125 s. Because there is a correlation between the data at adjacent periods, we estimated the correlation coefficients of residuals at different periods and transferred them to off-diagonal terms in the data covariance matrix,  $C_{nn}$  (note that we use the same notation for covariance matrices as in the earlier inversion for phase velocities, but the data and model parameters are different). For a given period, only the correlation to its first and second nearest neighbors was calculated. The correlation between two adjacent short periods is smaller than that between two longer periods, because the interference effects of multipathing that are not represented adequately by the two plane waves introduce uncorrelated “noise” that is more pronounced at short periods. The diagonal terms in  $C_{nn}$  are calculated from the standard errors of phase velocities. We used a modified version of the AK135 reference model [Kennett *et al.*, 1995] as a starting model (Figure 9). It contains 18 layers from the Earth’s surface to the bottom of the transition zone (660 km) with layer thickness ranging from 20 to 150 km. There is one model parameter in each layer, a scalar value that multiplies all the elastic coefficients in that layer by a constant. The initial value for the model parameters is 1.0 for all layers. If this model parameter is larger than 1.0 in the solution, it indicates that velocity in that layer is higher than that in the initial model. The initial  $V_p/V_s$  ratios are preserved in all layers. The partial derivatives relating the data and model parameters are numerically calculated using Thomson’s variational integral method [Martin and Thomson, 1997; Thomson, 1997]. We assigned an a priori error of 0.04 for elastic model parameters (corresponding to about 2% in velocity, which is proportional to the square root of the elastic coefficients) and introduced vertical smoothing through off-diagonal terms in  $C_{nn}$  equivalent to a correlation of 0.4 between a layer and its nearest neighbors. The change in model parameters is calculated using equation (2), except that now the data and model parameters correspond to phase velocities and elastic model scaling coefficients, respectively.

[27] Because model AK135 may not be an optimal starting model for our study area, we inverted for an improved 1-D model before solving for 3-D structure. To

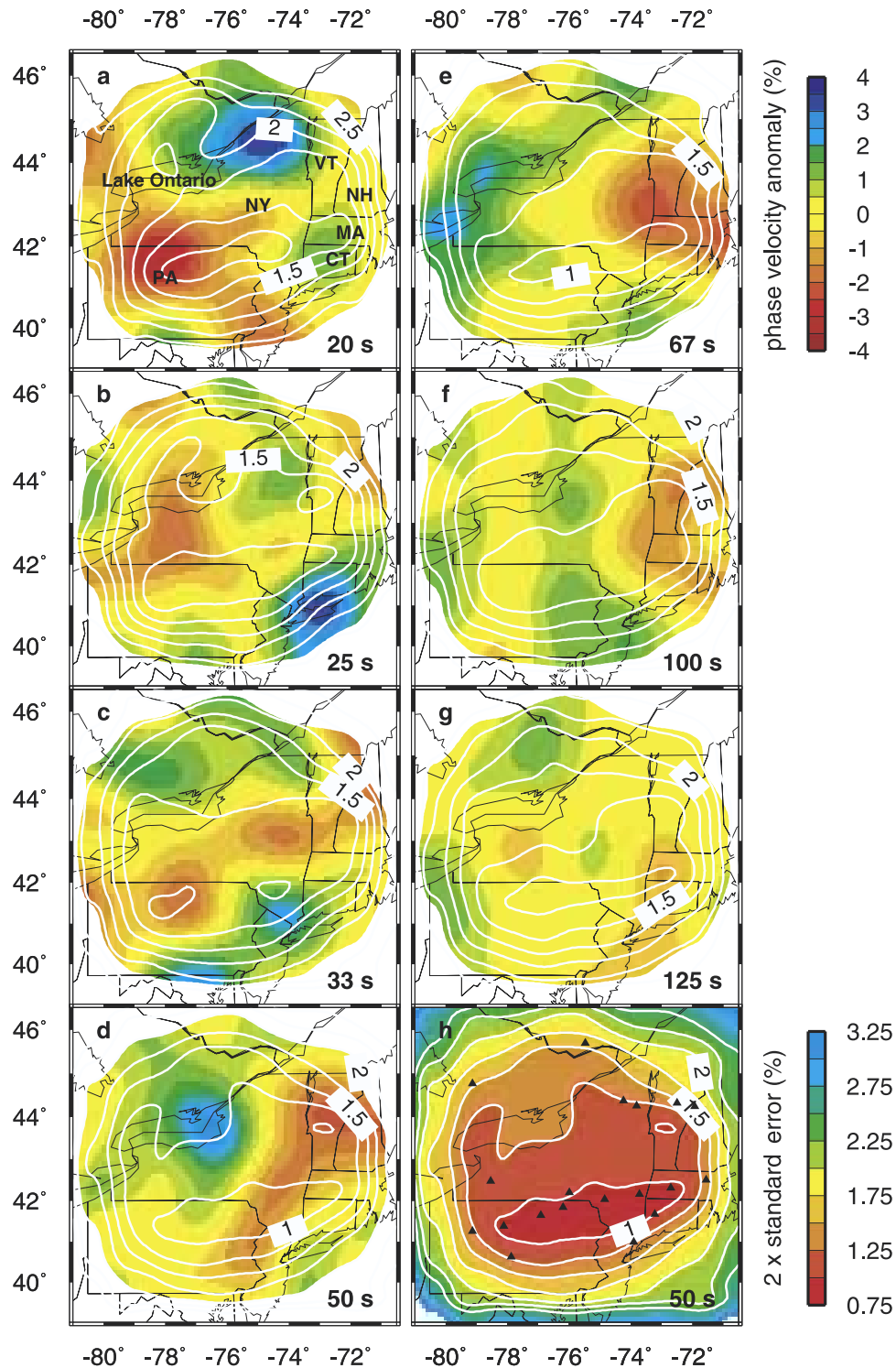


**Figure 8.** Maps of Rayleigh phase velocities and phase velocity uncertainties. The phase velocity maps are represented at seven periods: (a) 20 s, (b) 25 s, (c) 33 s, (d) 50 s, (e) 67 s, (f) 100 s, and (g) 125 s. Velocity anomalies were calculated relative to the average phase velocities shown in Figure 7. The open contours are twice the standard errors in percent of phase velocity anomalies at each period. The phase velocity maps are clipped by the 2% error contour at 50 s as shown in (Figure 8h), the uncertainty map of 50 s.

obtain a better starting model, we employed phase velocities from a point between MM02 and MM03 (Figure 1), where a crustal thickness of 41 km has been well constrained by receiver functions [Li *et al.*, 2002a] and the phase velocities

have the maximum resolution (Figure 8h). During the inversion, the predicted phase velocities were calculated for each updated model while the partial derivatives were kept the same as the starting values. One practical reason for

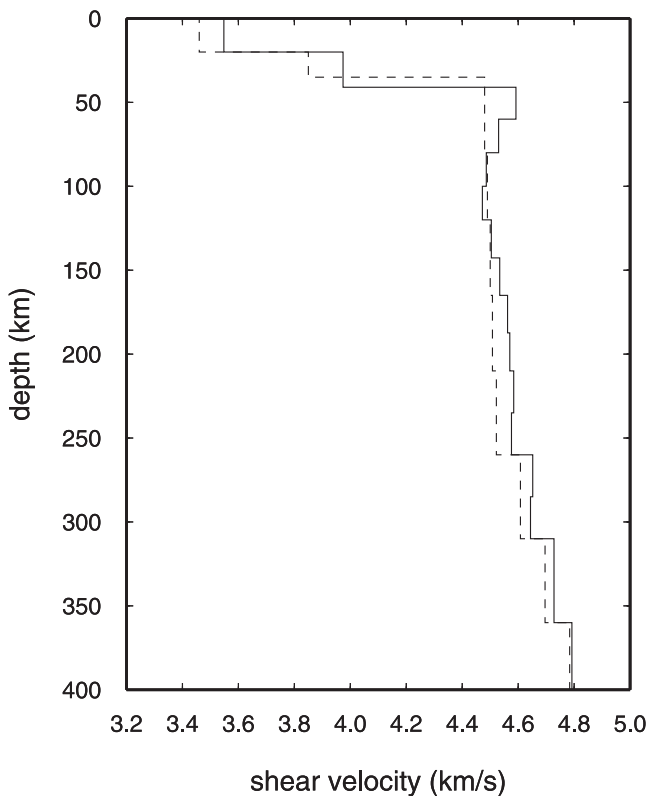


**Figure 9.** Initial models. The dashed line represents a modified AK135 model used as the original starting model. The solid line is the 1-D model obtained by inverting phase velocities at 74.3°W, 42.1°N, and subsequently used as the starting model for inversions throughout the area.

this is that it is computationally intensive to calculate partial derivatives for a given model. However, our experiments showed that the partial derivatives are not sensitive to small velocity changes in each layer for a constant crustal thickness. Velocity in the transition zone layer was fixed because our data do not contain much information at that depth.

[28]  $S$  wave velocity in the crustal layers of the improved 1-D model (Figure 9) is generally faster than in the initial starting model. A fast lid with a 2% anomaly appears beneath the Moho, and a weak, low-velocity zone lies beneath the lid. The higher velocities in the lower crust and uppermost mantle could have been modeled equally well by a thinner crust with velocities equal to AK135, but we choose to give preference to a priori information about crustal thickness from receiver functions [Li *et al.*, 2002a]. Velocity at depths of 150–300 km is higher than the initial model. Given the longest Rayleigh wave period at 125 s, we expect reasonable resolution down to 200 km depth. This improved 1-D velocity model was used as a starting model for 3-D structure inversions.

[29] The variation of crustal thickness in the area must be taken into account in order to more accurately resolve 3-D structure. Crustal thickness varies from 30 to 50 km across the MOMA array according to receiver function studies [Li *et al.*, 2002a] and 35–45 km in the refraction based model of Mooney and Braile [1989]. Such a big variation is significant and crustal thickness may trade-off with velocity structure in the crust and upper mantle if it is ignored.

Introducing crustal thickness as a model parameter makes the inversion nonlinear. The partial derivatives relating phase velocities and model parameters change substantially for models with different crustal thickness. Because of the long computational time in calculating the partial derivatives using finite differences between different forward models with Thomson’s code, we did not compute them at each iteration. Instead, we constructed a table of partial derivatives for 13 starting models which have the same velocity as the 1-D starting model (solid line in Figure 9) but different crustal thickness ranging from 28 to 52 km with an interval of 2 km. The crustal thickness increases at expense of the thickness of the uppermost mantle layer, and the thickness of the upper crust is held constant. After one iteration, a different set of partial derivatives is generated for the updated crustal thickness by interpolating the table of partial derivatives. Time spent on calculating for predicted phase velocities after each iteration also becomes a practical problem when inverting velocity structure for over 10,000 points on the map. To solve this problem, we estimated the predictions using Taylor expansions up to the second order. Therefore the second-order partial derivatives for different starting models are also calculated beforehand. The predicted phase velocities can be written as:

$$d_i^{k+1} = d_i^k + \sum_{j=1}^m g_{ij} \Delta m_j + \frac{1}{2} \sum_{j=1}^m g'_{ij} \Delta m_j^2, \quad (3)$$

where  $d_i^{k+1}$  and  $d_i^k$  are the  $i$ th synthetic phase velocity (ordered by frequency) at the  $(k+1)$ th and  $k$ th iteration, respectively,  $g_{ij}$  is the first and  $g'_{ij}$  the second partial derivative of the  $i$ th phase velocity with respect to the  $j$ th model parameter,  $\Delta m_j$  is the change in the  $j$ th model parameter, and  $m$  is the total number of model parameters. We neglected second-order derivatives involving model changes in two different layers. This approximation is reasonably accurate in comparison with numerically calculated phase velocities.

## 4.2. Crustal Structure

[30] Three-dimensional crustal structure is displayed in Figure 10. Shear wave velocity anomalies (Figures 10a and 10b) are relative to the 1-D improved model in Figure 9 which has an overall 2.1–2.7% faster crust than that in the AK135 model (Figure 9). Because phase velocities are related to both the crustal thickness and velocity structure, a trade-off between these parameters must be present. The maps presented here were found with damping created by assigning in  $C_{mm}$  a priori standard deviations of 8 km to crustal thickness and 0.04 to the elastic scaling parameter in each layer (corresponding to about 2% in velocity). Changing the damping in a reasonable range (5 ~ 10 km on the crustal thickness and 0.01 ~ 0.06 on elastic parameters) slightly changes the resultant crustal thickness (<3 km). There are about 1.4 independent pieces of information for crustal structure, ~0.8 for the crustal thickness and ~0.6 for the velocity. Therefore crustal thickness is relatively well resolved despite some trade-off with velocity in the crust and the top part of upper mantle.

[31] The velocity in the crust varies only slightly in most of the region with anomalies within  $\pm 0.5\%$  (yellow area). A circular fast anomaly appears between Lake Ontario and

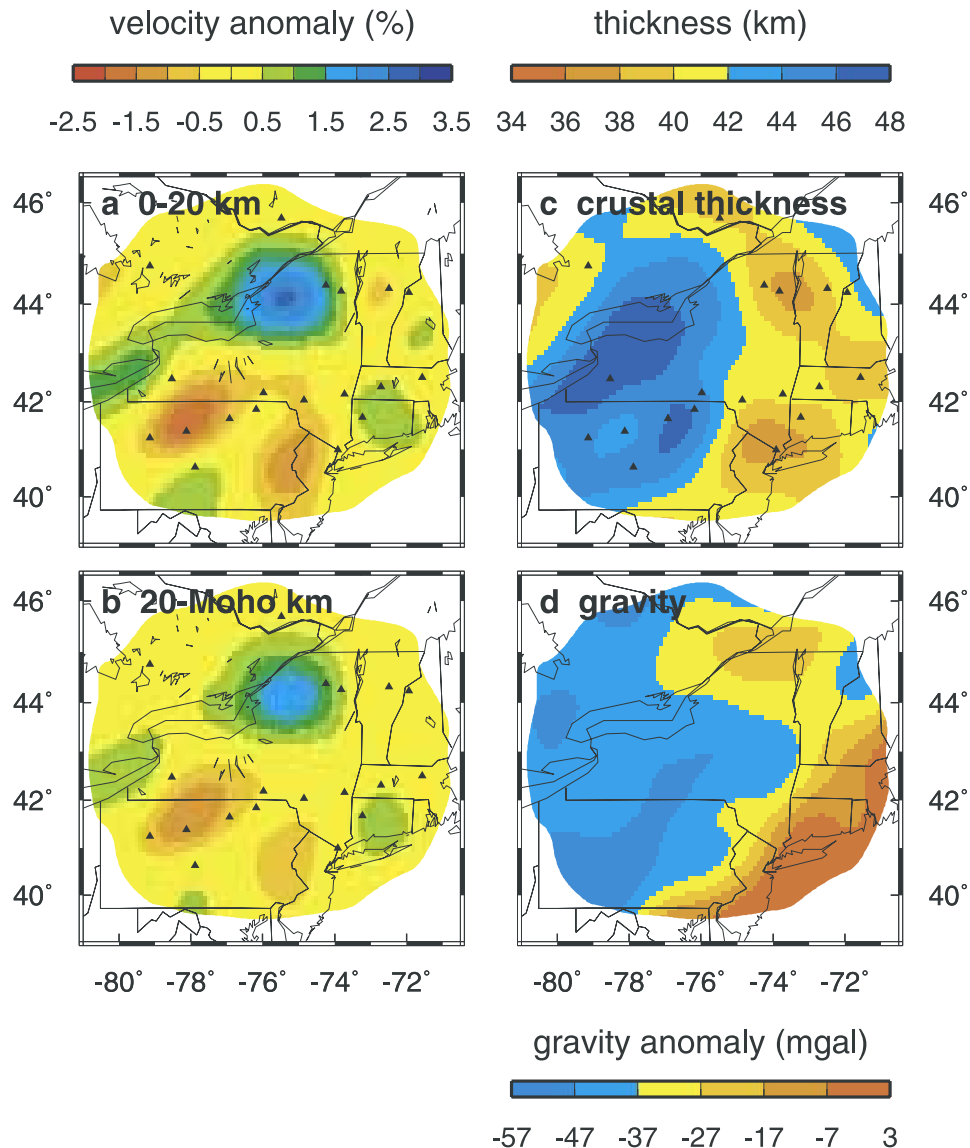


**Figure 10.** Maps of crustal velocity, crustal thickness, and gravity anomaly. (a) Shear wave velocity anomaly at depths of 0–20 km. (b) Shear wave velocity anomaly from 20 km to the Moho. Velocity anomalies are calculated relative to the improved 1-D model (solid line) in Figure 9. (c) Crustal thickness map obtained from Rayleigh wave phase velocities. (d) Map of gravity anomalies [Hittelman *et al.*, 1990]. Bouguer anomaly is shown for continent and free air anomaly for oceanic region.

Vermont (Figures 10a and 10b) and correlates well with the Adirondack Mountains. This observation is consistent with the fast  $P$  wave velocities throughout the crust [Hughes and Luetgert, 1991, 1992] and the fast  $S$  wave velocities in the upper crust [Musacchio *et al.*, 1997] found beneath the Adirondack Granulite terrane on the Ontario-New York-New England seismic profile.  $P$  and  $S$  wave tomography by Levin *et al.* [1995] and  $P$  wave tomography by Zhu and Ebel [1994] also suggested that the upper crust of the Proterozoic Grenville Province is, on average, faster than the Paleozoic Appalachians and the area of anorthositic intrusions within the Adirondack Mountains is even faster. Another obvious velocity anomaly in the crust is the elliptical slow area across the northern border of Pennsylvania, which is surrounded by several stations and should be well resolved. This area is part of the Appalachian basin

and on the Appalachian Foreland [Shumaker and Wilson, 1996]. A relatively thick sedimentary layer exists beneath MM04 to MM07 [Shumaker and Wilson, 1996; Li *et al.*, 2002a], which is probably responsible for the observed slow anomaly.

[32] Substantial variations in crustal thickness are also resolved in the inversion for 3-D structure from phase velocities. Relatively thin crust is observed along the Atlantic coast and the Appalachians in central and southern New England, whereas the crust beneath the western Appalachians in Pennsylvania and the Grenville Province in New York is thicker (Figure 10c). The crustal thickness in well-resolved areas varies from 36 km at the Atlantic coast in the east to 48 km in the interior of the Grenville Province, which is similar to the trend and range given by Mooney and Braile [1989]. This variation is smaller than that

observed by *Li et al.* [2002a] from receiver functions for the MOMA stations. The lateral resolution of surface waves is much poorer than that of receiver functions; extreme values will tend to be greater with any approach that yields finer resolution. The inversion of reflection data by *Hughes and Luetgert* [1991;1992] and *Mussachio et al.* [1997] also showed that the crust is thicker under the Adirondack Mountains and thinner beneath the New England Appalachians. There is some mismatch between the absolute values of crustal thickness between this study and previous observations by other techniques, but the overall patterns agree nicely.

[33] Crustal structure is reflected in gravity anomaly data following the simple rule that a negative Bouguer anomaly is associated with thicker or less-dense crust and a positive anomaly is associated with thinner or denser crust, although of course mantle density variations also play a role. The observed gravity anomalies (Figure 10d) are more positive along the Atlantic coast and in western Vermont and northern New York where the crust is thinner. More negative anomalies appear in the western Appalachians and the Grenville province where we observe thick crust. In general, the pattern of Bouguer anomaly at long wavelengths agrees well with the variation of crustal thickness in our model.

[34] Having obtained crustal structure from phase velocities, we compared our model with crustal structure constrained by receiver functions [*Li et al.*, 2002a]. Assuming a vertical ray path, we calculated *S-P* travel time delays from the Moho to the surface using the velocity model in Figure 10 and the *Li et al.* receiver function model. The calculation was done at eight stations, HRV and MM01 to MM07, where the constraints from receiver functions are available. The correlation between the predictions from the two models is generally good except at stations MM01 and HRV (Figure 11). HRV and MM01 are separated by  $\sim 100$  km, yet differed by 15 km in estimated crustal thickness from receiver function analysis. Such large and rapid variations of crustal structure are likely to be smoothed in the surface wave analysis. However, there is good agreement with the average of the values at the two sites (the open circle in Figure 11). The excellent agreement between models at MM02 and MM03 confirms that our starting model, which is at a point between these two stations, also largely satisfies the constraints from receiver functions.

### 4.3. Shear Wave Structure in the Upper Mantle

[35] Figure 12 shows shear wave velocity structure in eight layers from the Moho to 210 km depth. A key feature of upper mantle structure is the high-velocity, North American continental keel imaged beneath the Grenville Province down to roughly 200 km depth. This keel has been imaged in many previous tomography studies [*Grand*, 1994; *Alsina et al.*, 1996; *Grand et al.*, 1997; *Van der Lee and Nolet*, 1997; *Larson and Ekstrom*, 2001]. The model of *Van der Lee and Nolet* [1997] contains a low-velocity dent in the eastern edge of the keel, which was not seen as prominently in other models. Here we also find evidence for irregular morphology in the eastern edge of the keel and are able to see how the keel depth varies laterally.

[36] From the Moho to  $\sim 140$  km (Figures 12a–12e), a smooth boundary with strong velocity gradients separates

fast velocity anomalies in the north and west of the area from generally slow anomalies in the central east. The smooth keel edge begins to disappear at depths of 140–165 km (Figure 12f) and a coherent, fast “keel-like” feature vanishes at greater depth (Figures 12g and 12h). Fast velocity anomalies are also observed in the southeast corner of the area at depths of 60–140 km, but these small-scale fast anomalies are not robust owing to the poor resolution at the edges of the map area.

[37] A prominent slow anomaly is imaged beneath eastern New York and central New England from the Moho to 200 km with particularly high amplitudes at depths of 60–140 km. However, since resolution decreases with increasing depth in our model, care must be taken not to overinterpret small-scale or low-amplitude variations in velocity. At each point in the maps, the phase velocities from 20 to 125 s typically provide  $\sim 3$  pieces of independent information, including  $\sim 1.4$  for shear wave velocity structure in the upper mantle. (More vertical information is provided by the average dispersion curve shown in Figure 7 for the region as a whole, which has smaller standard errors.) Therefore lateral heterogeneity averaged over a vertical depth range of less than 50 km is unlikely to be resolved. One standard deviation for velocity variation is about 0.5% when averaged from the Moho to 165 km, suggesting that velocity anomalies larger than 1.0% over this depth range are significant at the 95% confidence level. Broadly speaking, these results are similar to the model results of *Van der Lee and Nolet* [1997] and *Van der Lee* [2002], although some details of the models differ. At depths of roughly 100 km, both models place the edge of the keel in roughly the same location. At depths of roughly 200 km, the entire region where we resolve shear wave velocity with the exception of the southwest corner of Pennsylvania falls inside the broad V-shaped-indentation slow anomaly imaged at these depths by *Van der Lee and Nolet* [1997]. The absolute velocities we see at these depths are not quite as low as those obtained by *Van der Lee and Nolet*, but the models agree in the sense that neither resolves fast keel-like material over most of this mantle volume. *Levin et al.* [2000] also resolve a low velocity of comparable amplitude to that found in our model, although with a somewhat different shape.

[38] The North America keel in this region has survived over a billion years since the end of the Grenville orogeny, but its irregular shape and the pronounced low-velocity zone to the east raise the possibility of at least some lithosphere modification. Shear wave velocity profiles through several cross sections (Figure 13) allow us to view the variations of the keel depth and the keel shape from a different perspective. The fast keel is imaged to the west of  $75^\circ\text{W}$  and the slow oceanic-like mantle to the east (Figures 13a and 13b). Defining a particular depth to the base of the keel is difficult, given the limited vertical resolution. If the base of the keel is defined as the depth to which anomalously fast velocities extend, then there is a tendency to overestimate its extent due to vertical smearing. We estimate that the velocity contrast between the western fast region and eastern slow region must extend to at least about 150 km depth, although if there is no sharp contrast at its base, then it could be as deep as the maximum depth of anomalies shown in the figure. There are suggestions of contrasts to depths greater than 200 km in some parts of the model (Figure 13b). However, because

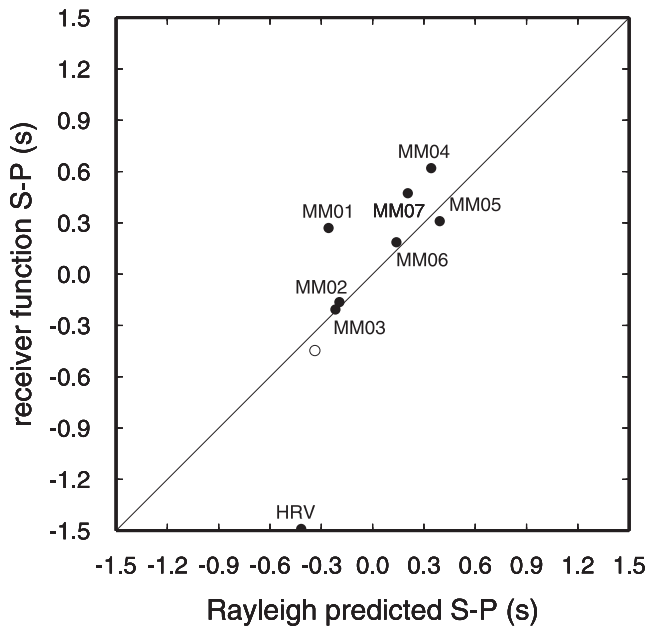


**Figure 11.** Correlation of  $S$ - $P$  travel times after removing mean values through the velocity models resolved from Rayleigh waves ( $X$  axis) and the models constrained from receiver functions ( $Y$  axis) [Li *et al.*, 2002a]. A vertical ray path was assumed for the calculations. The open circle indicates the average of  $S$ - $P$  travel times at stations HRV and MM01. Station names are plotted close to the corresponding values.

there could be velocity differences within the asthenosphere, defining the extent of the lithosphere on this basis is not entirely satisfactory.

[39] If, instead, the depth to the maximum negative velocity gradient is chosen as the criterion for picking the base of the lithosphere, with limited vertical resolution the result will be dependent on gradients present in the starting model and on the decreasing ability to resolve sharp gradients with increasing depth. The velocity anomalies in Figure 13 need to be added to the starting model shown in Figure 9 to estimate the true gradients. The starting model has negative gradients down to about 100 km and positive gradients at depths greater than 120 km; therefore in the eastern, low-velocity region, the gradient-defined depth to the bottom of the lithosphere is significantly less than 100 km, probably 70–80 km in the center of the region. In the western, fast region, the depth to the maximum negative gradient is somewhat variable and hard to define because the low-velocity region is not very pronounced, but generally lies in the 100–150 km range.

[40] At 42°N (Figure 13b), the shape of the deep velocity anomaly at the edge of the keel at 75°–76°W, although only marginally resolved, is reminiscent of the edge-driven, small-scale downwelling modeled by King and Ritsema [2000]. More convincing as the effect of convection in the upper mantle is the thin lithosphere beneath west-central New England and easternmost New York, which may be caused by thermal erosion associated with the Monteregian hotspot that passed over this area around 100–120 m.y. ago [Crough, 1981; Morgan, 1983; Sleep, 1990; Heaman and

Kjarsgaard, 2000] (Figure 12). Low velocities continue along the hotspot track into the Atlantic Ocean in the model obtained by Van der Lee and Nolet [1997]. Small-scale thermal erosion of continental keels by hotspot plumes has also been invoked in other regions. Rondenay *et al.* [2000] explained a narrow low-velocity zone they observed at roughly 78°W, 46°N by interaction of the Monteregian hotspot with a weak zone in the cratonic lithosphere, and vanDecar *et al.* [1995] imaged a slow anomaly in the lithosphere beneath the Brazilian craton which they interpreted as a fossil plume.

[41] Shear velocity in the slowest region is about 5.5% lower than in the keel and 2% lower than that in the immediately surrounding mantle. Given that a 100°C increase in temperature decreases the shear velocity in the shallow mantle by ~1.1% [Nataf and Ricard, 1996], the slow region would be about 200°C hotter than the surrounding mantle and 500°C hotter than the lithospheric keel if the anomaly is purely thermal in origin. This would be a large temperature contrast if it were located solely in asthenosphere. For example, an active hotspot such as Iceland appears to be associated with ~200°C thermal anomaly [Wolfe and Solomon, 1998]. However, most of the velocity contrast lies at depths shallower than 150 km, with the maximum at about 100 km. Thus we are primarily seeing the lateral contrast between the relatively thick lithosphere beneath western New York and Pennsylvania and the warm asthenosphere beneath the thinned New England lithosphere. The temperature contrast required is not unreasonable, but there could also be contributions from other sources. Van der Lee and Nolet [1997] suggested that the low velocities represent water in the mantle associated with the subduction of the Iapetus plate on the order of 400 m.y. ago, perhaps combined with melting related to the Monteregian plume. However, because water tends to partition into melt, hotspot magmatism or melting related to the Jurassic opening of the Atlantic Ocean [Rankin, 1994] would tend to remove water from the shallow mantle. Alternatively, Levin *et al.* [2000] and Park and Levin [2002] suggested that the slow velocities represent iron-rich asthenosphere that replaced delaminated lithosphere beneath the Appalachians and then subsequently became part of the lithosphere through cooling and dehydration. However, this hypothesis does not easily explain the continuation of the slow anomaly into the Atlantic Ocean.

## 5. Azimuthal Anisotropy

### 5.1. Observations From Surface Waves

[42] Azimuthal anisotropy in eastern North America has been documented in numerous shear wave splitting studies [Vinnik *et al.*, 1992; Silver, 1996; Barruol *et al.*, 1997; Levin *et al.*, 1999; Fouch *et al.*, 2000; Rondenay *et al.*, 2000]. Shear wave splitting data have good lateral resolution and can reveal differences in anisotropy between closely spaced stations. However, shear wave splitting alone cannot tell where anisotropy is located along ray paths due to the lack of vertical resolution. Taking advantage of the surface wave property that data at different periods sample velocity structure over different depth ranges, it is possible for us to constrain the distribution of anisotropy with depth.

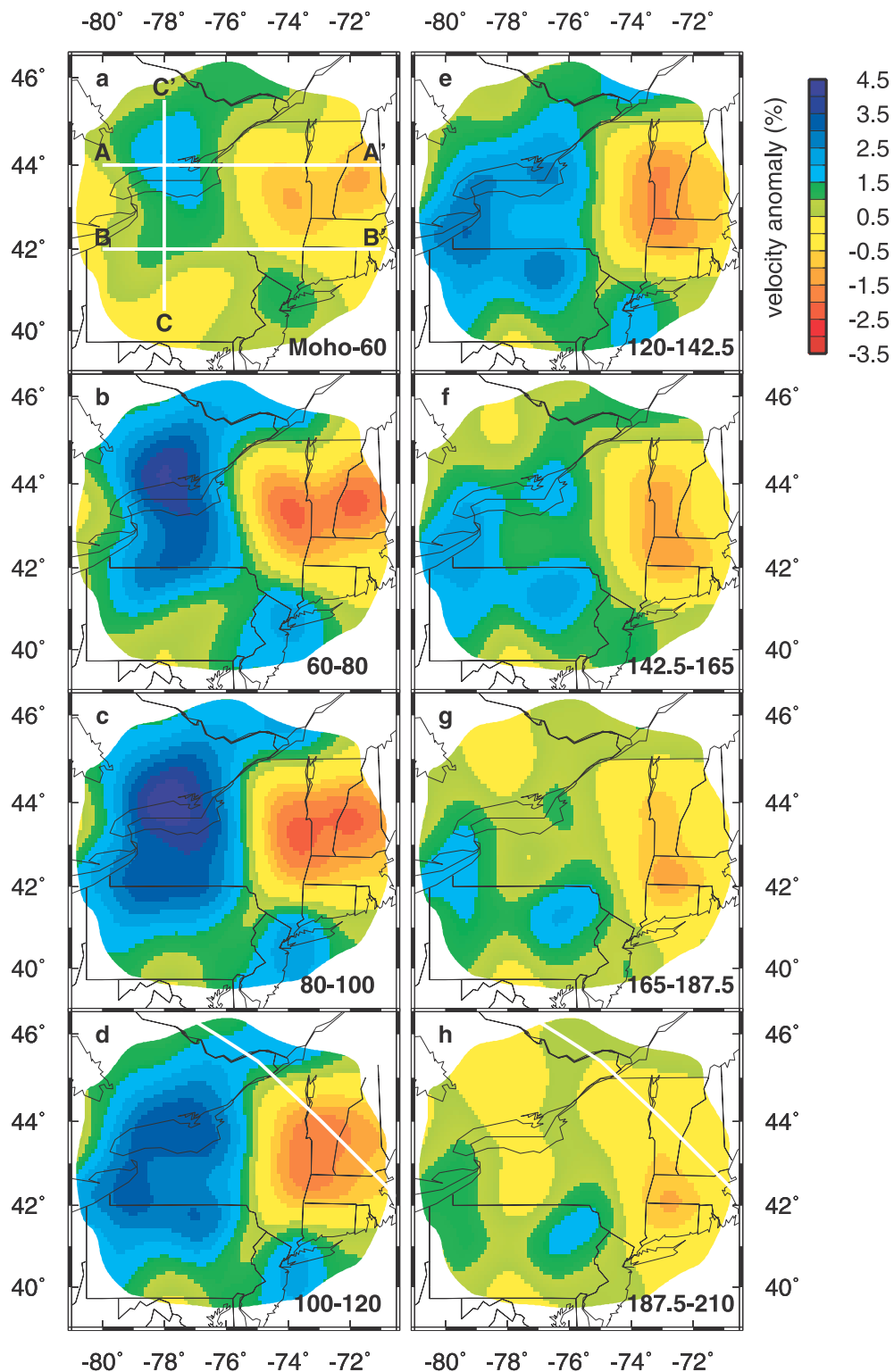


**Figure 12.** Maps of isotropic shear wave velocity anomaly in eight layers from the Moho to 210 km. The velocity anomaly is relative to the improved 1-D model (solid line) in Figure 9. The maps are clipped in the same way as in Figure 8 for phase velocity maps. The open contours in 12a are locations of vertical profiles in Figure 13, and the open contour in Figures 12d and 12h represents the track of the Great Meteor hotspot [Crough, 1981; Heaman and Kjarsgaard, 2000].

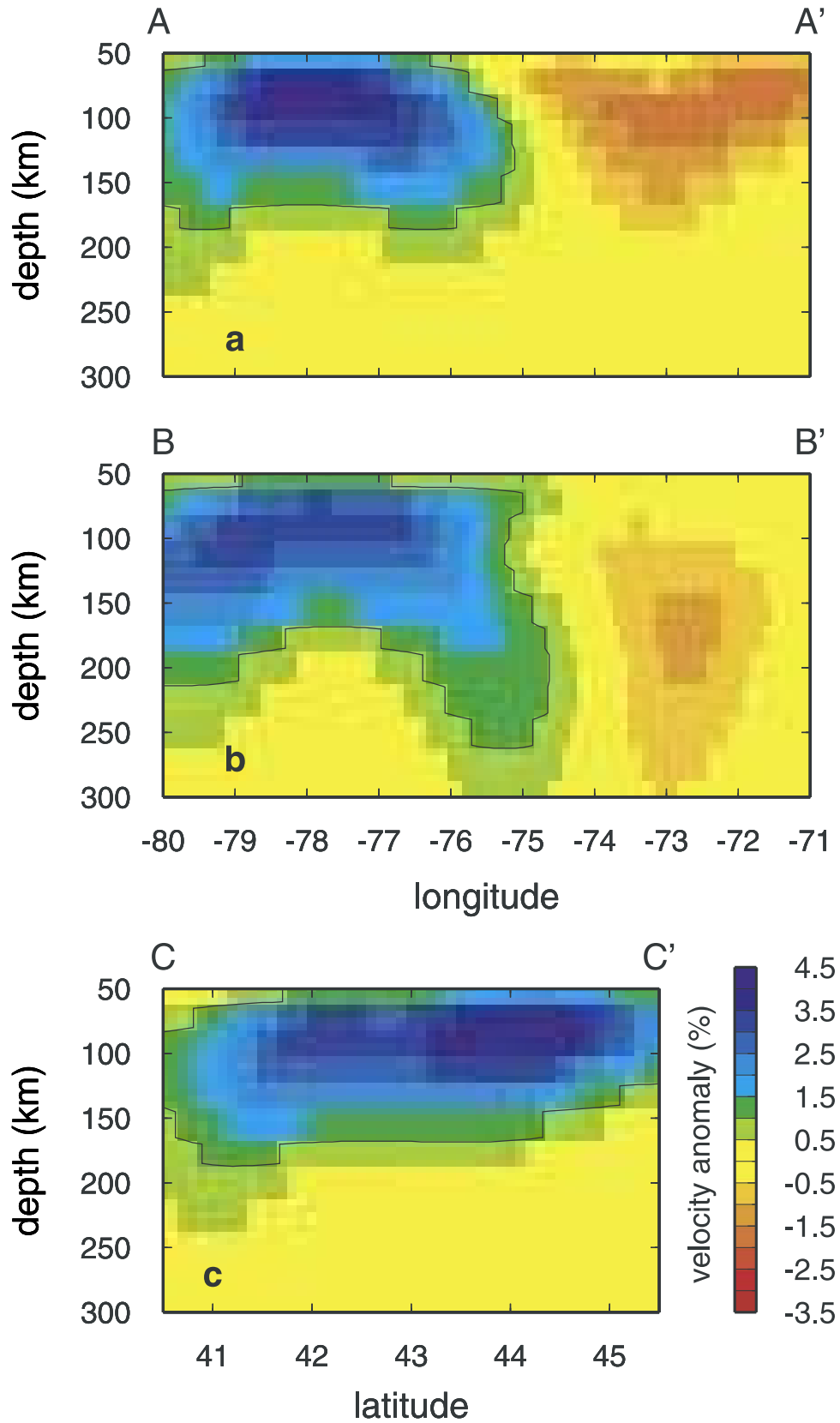


**Figure 13.** Vertical profiles of shear wave velocity structure. The locations of the three profiles are shown in Figure 12a. Solid lines delineate the contour of 1% velocity anomaly.

[43] Although lateral changes in shear wave splitting occur in this region, shear wave splitting variation within the array used for the Rayleigh wave inversion is relatively small (Figure 4) [Fouch *et al.*, 2000; Levin *et al.*, 2000]. To start with a simple model, we assumed that anisotropy is uniform in the study area but allowed the isotropic term ( $B_0$  in equation (1)) to vary in two dimensions. We applied the inversion to nine periods from 33 to 125 s, which are primarily sensitive to structure in the upper mantle above a depth of about 300 km. The amplitude of anisotropy and its fast direction are computed from coefficients of isotropic and anisotropic terms in equation (1) at each period. The peak-to-peak anisotropy is  $2(B_1(\omega)^2 + B_2(\omega)^2)^{1/2}/B_0(\omega)$ , and the fast direction is  $0.5 \tan^{-1}(B_2(\omega)/B_1(\omega))$ . Standard deviations for the size and fast direction of anisotropy are estimated from the variance of  $B_1(\omega)$  and  $B_2(\omega)$  using an error propagation technique [Clifford, 1973].

[44] Anisotropy, if assumed uniform in the study area, is generally small, not significantly different from zero except at the longest period (Figure 14a), and although they are poorly constrained, the fast directions are at high angles to the fast directions for shear wave splitting. If Rayleigh wave azimuthal anisotropy and shear wave splitting both arise from orthorhombic or lower-order intrinsic anisotropy with a horizontal symmetry axis, the fast directions should coincide. In addition, our synthetic resolution tests indicate that the poorer coverage at the longest period could artificially increase the apparent azimuthal anisotropy. We conclude that the average azimuthal anisotropy in the area is small, well resolved to be less than 1%.

[45] There are several possible interpretations for the apparently weak anisotropy. First, the anisotropy in the depth range of sensitivity may really be weak, with the anisotropy responsible for the shear wave splitting too deep to resolve. Second, two or more anisotropic layers with different fast directions may coexist [e.g., Levin *et al.*, 1999, 2000] in such a way that the effects of the two layers tend to cancel each other through the vertical integration of Rayleigh waves over the depth range of sensitivity. Third, anisotropy at a given period may not be spatially uniform, with different directions of anisotropy that could destructively interfere when integrated over the entire study area. Some splitting measurements do manifest lateral variability [e.g., Barruol *et al.*, 1997; Fouch *et al.*, 2000; Rondenay *et al.*, 2000], and regardless of their pattern shear wave splitting measurements at different stations may reflect anisotropy in different depth ranges. We explore each of these possibilities in the paragraphs below.

[46] Ideally, to account for 3-D variations of anisotropy, the best method would be to solve for phase velocities allowing anisotropy to vary in two dimensions at individual periods and to invert for 3-D anisotropic velocity structure from phase velocities. However, our experiments show that 2-D anisotropic phase velocities are poorly constrained in most areas. These results are not surprising because of the large number of model parameters, which is three times that for the isotropic inversion. To reduce the number of model parameters and yet still account for some lateral variation of anisotropy, we divided the study area into subregions and assumed that the anisotropy is uniform in each subregion.

This assumption significantly reduces the model parameters needed to represent the anisotropic terms of phase velocity at each period.

[47] The subregions can be constructed based on tectonic provinces, patterns of shear wave splitting observations, or the isotropic structure in the upper mantle. Although we tried a variety of subdivisions, in the results shown here we assumed that anisotropy is uniform in just two subregions: the zone of fast isotropic velocities that we interpret as thick lithosphere and the area of prominent low velocities beneath eastern New York and New England (Figure 12). Some variation in observed shear wave splitting does occur within each of these subregions (Figure 4), but it is relatively small and any corresponding variation in anisotropy would likely be averaged out in the Rayleigh wave inversion. The variations of azimuthal anisotropy versus period for the two subregions are plotted in Figures 14b and 14c. The estimates of anisotropy are larger than in the uniform case (Figure 14a), but the uncertainties are also larger; the only individual periods that appear to have statistically significant azimuthal anisotropy are 40 s for the eastern region (Figure 14c) and the two longest periods for the western region. By pure chance, we would expect one of these values to appear significant at the 95% confidence level even if the true anisotropy were zero. The large jump in apparent anisotropy at the longest periods in the western region is physically unrealistic, given the overlapping depth range of sensitivity of adjacent periods. The fast directions in the two subregions are approximately orthogonal, which could simply be an inversion artifact. Although the fast direction in the eastern subregion at periods greater than 50 s (N108°E) is roughly in agreement with the shear wave splitting direction in that area, the average direction in the western region (N20°E) is rotated about 45° counterclockwise from the absolute plate motion direction and the average direction of shear wave splitting in western New York, western Pennsylvania, and southern Ontario (Figure 4). In summary, the resolution for azimuthal anisotropy in subregions is relatively poor, leaving open the possibility that there is significant anisotropy in different areas that could cancel when averaged over the entire study area, but we see no positive indication that such anisotropy exists.

[48] Assuming then that there is no resolvable lateral variation in anisotropy, to constrain the possible depth range of anisotropy, we constructed several forward anisotropic models that produce shear wave splitting matching the observed average to compare to the Rayleigh wave observations. Four models and corresponding predicted azimuthal anisotropy are shown in Figure 15. All models contain an isotropic crust and the degree of anisotropy in the mantle is chosen so that predicted splitting delay times are about 0.9 s, the average value in the study area from observed shear wave splitting. Anisotropy in the mantle anisotropic layers is represented as 70% olivine and 30% orthopyroxene [Babuska and Cara, 1991]. Elastic coefficients in each layer are written as  $C_{ijkl} = \alpha[\varepsilon C_{ijkl}^{\text{aniso}} + (1 - \varepsilon)C_{ijkl}^{\text{iso}}]$ , where  $\varepsilon$  is the fraction of olivine  $a$ - and orthopyroxene  $c$ -axes aligned in the fast direction assuming that olivine  $a$ - $b$  and orthopyroxene  $a$ - $c$  planes are horizontal. The remaining fraction is randomly oriented in 3-D. The  $\alpha$  is a scalar value used to multiply elastic coefficients in each layer to

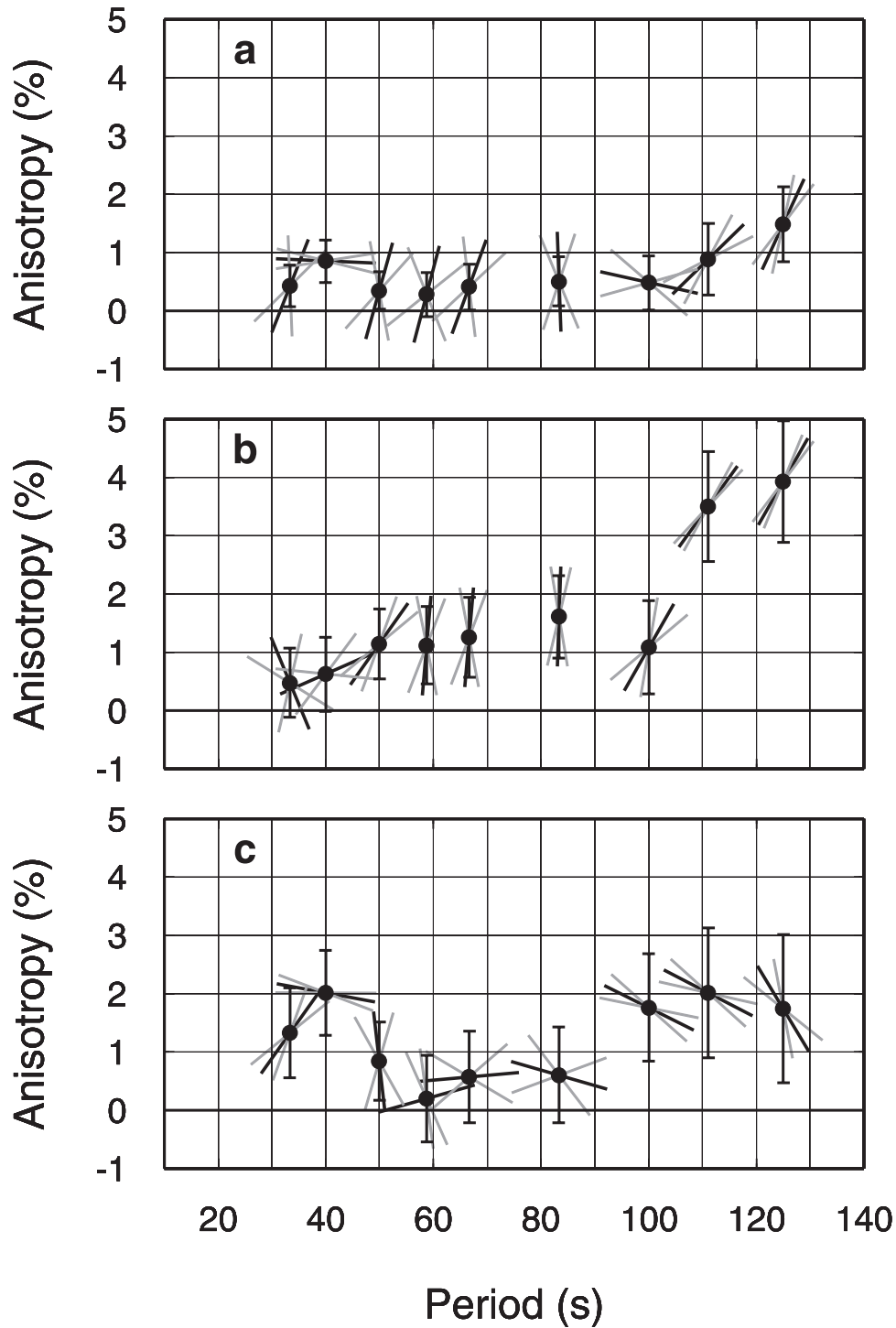


**Figure 14.** Variations of azimuthal anisotropy with period. (a) Amplitudes and directions of average anisotropy in the whole study area. (b) Same as Figure 14a but for the high-velocity area shown in Figures 12b–12d. (c) Same as Figure 14a but for the low-velocity area shown in Figures 12b–12d. The vertical solid bars with caps represent one standard deviation of amplitude. Slanted solid bars show the fast directions as if from a map view with the positive  $Y$ -axis north; one standard deviation for the fast direction is shown as two shaded bars at each period. The thick horizontal line indicates zero anisotropy.

reflect isotropic changes due to thermal, pressure, or compositional effects, scaled so that average  $S$  velocity is equal to the  $S$  velocity in each layer of our isotropic starting model. Synthetic phase velocities,  $c(\omega, \psi)$ , are computed

using Thomson's method [Martin and Thomson, 1997; Thomson, 1997]. Synthetic delay times and fast directions are calculated based on the analytic method of Montagner and Griot-Pommeret [2000].

[49] In model 1 (Figure 15), anisotropy was limited to lithospheric depths above 165 km. Predictions from model 1 show that azimuthal anisotropy would be about 2% at periods of 33–60 s and would gradually decrease to ~1% at longer periods. Azimuthal variations of this size would have been detected easily at all periods less than about 100 s. In model 2, anisotropy is constrained to the depth range of 165–310 km. This model predicts that the strength of azimuthal anisotropy increases from near zero at 33 s to ~1% at 100–125 s, which would be below the detection threshold at short periods and marginally detectable in the 80–125 s range. The predicted values are larger than we observed from 80 to 100 s (and of course the directions do not agree well), but given the uncertainties in the observations, our data could be compatible with the prediction within 95% confidence limits. In model 3, the predicted anisotropy is less than 0.5% for all periods because Rayleigh waves at periods up to 125 s are relatively insensitive to structure at depths greater than 300 km. The fourth model with uniform anisotropy in the whole upper mantle from Moho to 410 km predicts azimuthal anisotropy between 0.6 and 1% increasing slightly with period. The amplitude of predicted anisotropy in this model is larger than the observed amplitude in the 50–100 s range, but within the 95% confidence limits of each individual measurement. However, since the observations at each period we portray are nearly statistically independent of each other, based on an analysis of the covariance between travel time residuals, if this model were correct we would expect the fast direction averaged over all periods to agree with the E-W splitting direction. Thus we conclude that if anisotropy were distributed as in model 4, it should have been detected and was not. Based on these models, we conclude that the anisotropy responsible for shear wave splitting cannot be concentrated primarily within the lithosphere and that much of the anisotropic structure must be deeper than 250 km.

[50] Finally, we test the possibility that vertical variations in anisotropy could serve to prevent the detection of the anisotropic structure by Rayleigh waves. *Levin et al.* [1999, 2000] postulated a two-layer anisotropic model beneath the northeastern United States based on azimuthal variations in shear wave splitting. In the limit, as the degree of intrinsic anisotropy becomes extremely large, the anisotropic layers could be very thin and still produce substantial shear wave splitting. Two such thin layers, closely spaced in depth and with fast directions orthogonal to each other would be undetectable by any means, such as surface wave dispersion, that averages over a depth range much greater than the vertical extent of the two layers. We test whether it is physically reasonable for the layers to be undetectably thin and whether the layers suggested by *Levin et al.* are sufficiently orthogonal to escape detection.

[51] In our forward models, we adopt the fast directions and maximum delay times at station HRV from *Levin et al.* [1999] for the top (N115°E, 0.7 s) and bottom (N53°E, 1.1 s) anisotropic layers, but allow the thickness of the two layers to vary. Figure 16 shows four models and predicted azimuthal anisotropy from these models. Model 1 duplicates the layer thickness, orientation, and shear wave splitting of the preferred orthorhombic model of

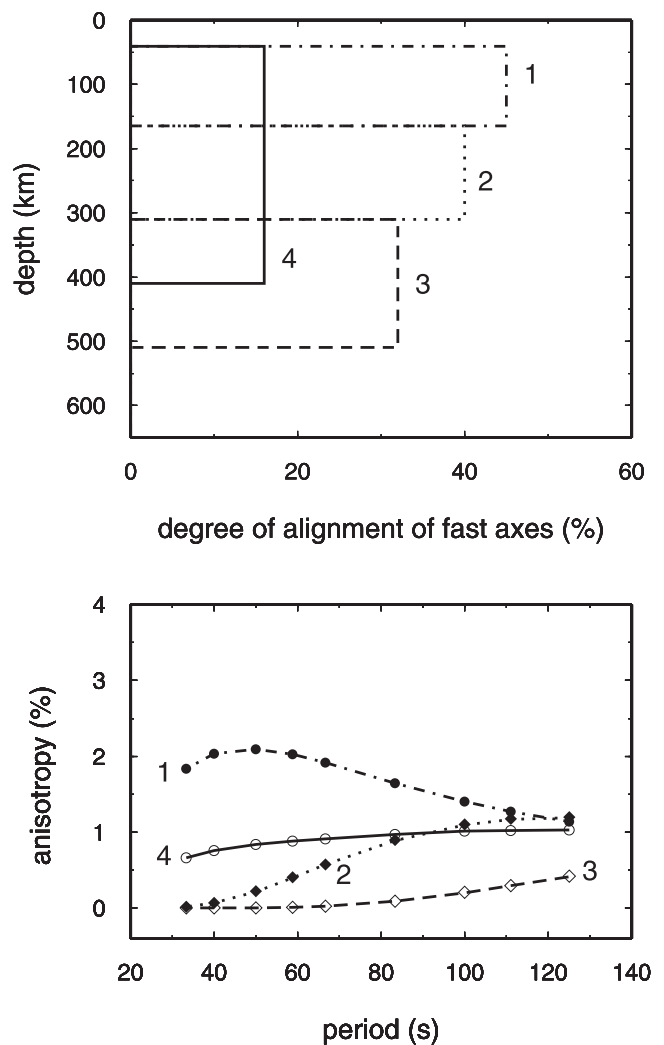


**Figure 15.** One-layer anisotropic models and predicted azimuthal anisotropy. In each model, anisotropy is uniformly distributed in a given depth range. (top) Variations of percentage alignment of fast axes with depth for four different models. (bottom) Amplitude of predicted anisotropy corresponding to the models above.

*Levin et al.*, but we add pyroxene to their purely olivine model. The addition of pyroxene dilutes the anisotropic effect, requiring a greater degree of alignment to produce the same amount of splitting. Azimuthal anisotropy of Rayleigh waves should be easily detectable in this model, reaching a maximum of more than 2% at the shortest periods where the fast direction should be aligned in the direction of the fast direction in the upper layer. Although fast directions in the two layers are misoriented relative to each other by 62°, they are not sufficiently orthogonal to create more than a slight minimum in degree of azimuthal anisotropy in the transition between short periods that are sensitive predominantly to the shallow layer and longer periods that are sensitive mostly to the deeper layer. The interference cannot be increased significantly by making the layers thinner because the degree of alignment already approaches the limit. The interference reduces the azimuthal anisotropy somewhat, but these models demon-

strate that if the upper anisotropic layer begins at the Moho, it should produce a detectable effect on Rayleigh waves unless it extends deeper than 300 km. The predicted anomaly is undetectable and therefore compatible with our observations only if a large fraction of the anisotropic sources for shear wave splitting are at depths greater than 200 km.

## 5.2. Trade-Off Between Heterogeneity and Anisotropy

[52] A key issue when interpreting both isotropic and anisotropic models obtained in this study is the possibility that significant trade-off exists between lateral heterogeneity in isotropic velocity and the parameters for azimuthal anisotropy. Any azimuthal variation in velocity inferred from travel times, as in our experiment, can always be equally well represented by lateral heterogeneities if the heterogeneities are large enough and on short enough length scales. Usually, this requires unreasonably large velocity variations on the scale of the separation between stations; we confine our analysis to lateral variations on the scale allowed by our Gaussian smoothing parameter  $L_w$ .

[53] We conducted a series of synthetic experiments at a range of periods to assess the trade-off between lateral heterogeneity and azimuthal anisotropy. Using the same event and station information as in the real data, synthetic phases and amplitudes of Rayleigh waves were generated from isotropic phase velocity models that are based on the observed phase velocity maps in Figure 8. Using these synthetic data, we performed inversions for isotropic phase velocity and anisotropic phase velocities that are either uniform over the whole study region or that are allowed to vary between the two subregions.

[54] If the synthetic data are noise free, the input isotropic model can be perfectly recovered even at periods greater than 100 s and the artificial anisotropy is almost zero whether it is assumed to be uniform over the entire region or allowed to vary between the two subregions. If random noise is added to the synthetic data, the pattern of phase velocity anomalies in the input model is reasonably well retrieved but the size of the anomaly could be biased. In addition, some artificial anisotropy is introduced in the solution due to the trade-off with lateral heterogeneity. The artificial anisotropy when two subregions are introduced usually appears stronger than that in the whole area, indicating the trade-off of anisotropy between different regions, much as is reported in Figure 14. The fast directions in the two subregions are usually at an angle larger than  $45^\circ$  but not always orthogonal to each other. The resulting magnitudes and fast directions of this artificial “trade-off” anisotropy do not consistently match the observed Rayleigh wave results, varying with each different random noise input. In general, the results agree with the linearized estimates of error used in this paper, but there is an indication that the uncertainty in azimuthal anisotropy at the longest periods where azimuthal coverage is weakest may be underestimated.

[55] These experiments suggest that the pattern of isotropic phase velocity variation is better resolved than anisotropy. Artificial anisotropy is generated by the trade-off with lateral heterogeneity and the trade-off of anisotropy between different subregions, which are significant especially at long periods ( $>100$  s). Therefore interpreting the details of either the isotropic anomaly or the anisotropy at levels

below the indicated confidence limits is suspect. Because the amplitude of azimuthal anisotropy is small in this area, neglecting it introduces little error into the maps of isotropic variations in velocity at the scale lengths allowed by the Gaussian averaging function.

## 5.3. Discussion

[56] We detect no convincing pattern of azimuthal anisotropy with Rayleigh waves. Our observations and synthetic tests limit the amplitude of azimuthal anisotropy that could be hidden to be less than 1% at periods less than 100 s. Because these periods are sensitive to structure at depths up to 200 km, we can place strong constraints on the possible depth of anisotropy responsible for the clear and relatively uniform shear wave splitting pattern in the northeastern United States. We would have liked to detect the anisotropic layer in a positive sense, so that the variation with period could give even stronger constraints than our negative evidence, but nevertheless, the negative evidence that anisotropy in the upper 200 km of the mantle must be unresolvably small should not be ignored. Synthetic calculations indicate that the improved coverage that will be provided by USArray may decrease the errors to the point where the change in anisotropy with period would be well constrained.

[57] The origin of shear wave splitting beneath eastern North America has been vigorously debated for over a decade. Three primary hypotheses exist: fossil strain in the lithosphere due to the last regional tectonic event [e.g., *Silver, 1996*], shearing by sublithospheric mantle flow [e.g., *Vinnik et al., 1992*], and some combination of both [e.g., *Levin et al., 1999; Fouch et al., 2000*]. At this point, we have resolved that the anisotropy in the northeastern United States cannot be confined to the lithosphere, but most of our study region lies outside the area of thickest continental keel [*Van der Lee and Nolet, 1997*]. *Jordan [1978]* proposed that stable continental keels are transported coherently during plate movement, a model that has since been supported by roughly synchronous ages for crustal and mantle xenoliths in several regions [e.g., *Pearson et al., 1995*]. However, whether a decoupling zone of concentrated shear strain exists beneath continental keels remains an open question, awaiting resolution from station coverage such as that expected for the USArray. In several other regions where surface wave data have suggested the presence of azimuthal anisotropy at sublithospheric depths, such as beneath the Colorado Rockies [*Li et al., 2003*] and Australia [*Debayle and Kennett, 2000; Simons et al., 2002*], the fast direction of anisotropy tends to be parallel to the direction of absolute plate motion. These results support the presence of a sublithospheric shear zone that reflects at least partial decoupling between the motion of the lithosphere and the deeper mantle.

## 6. Conclusions

[58] Using Rayleigh wave phase and amplitude data, we have obtained shear wave structure and azimuthal anisotropy in the northeastern US and southeastern Canada. The conclusions of this study relate to the isotropic structure of the crust, and isotropic heterogeneity and azimuthal anisotropy in the mantle.

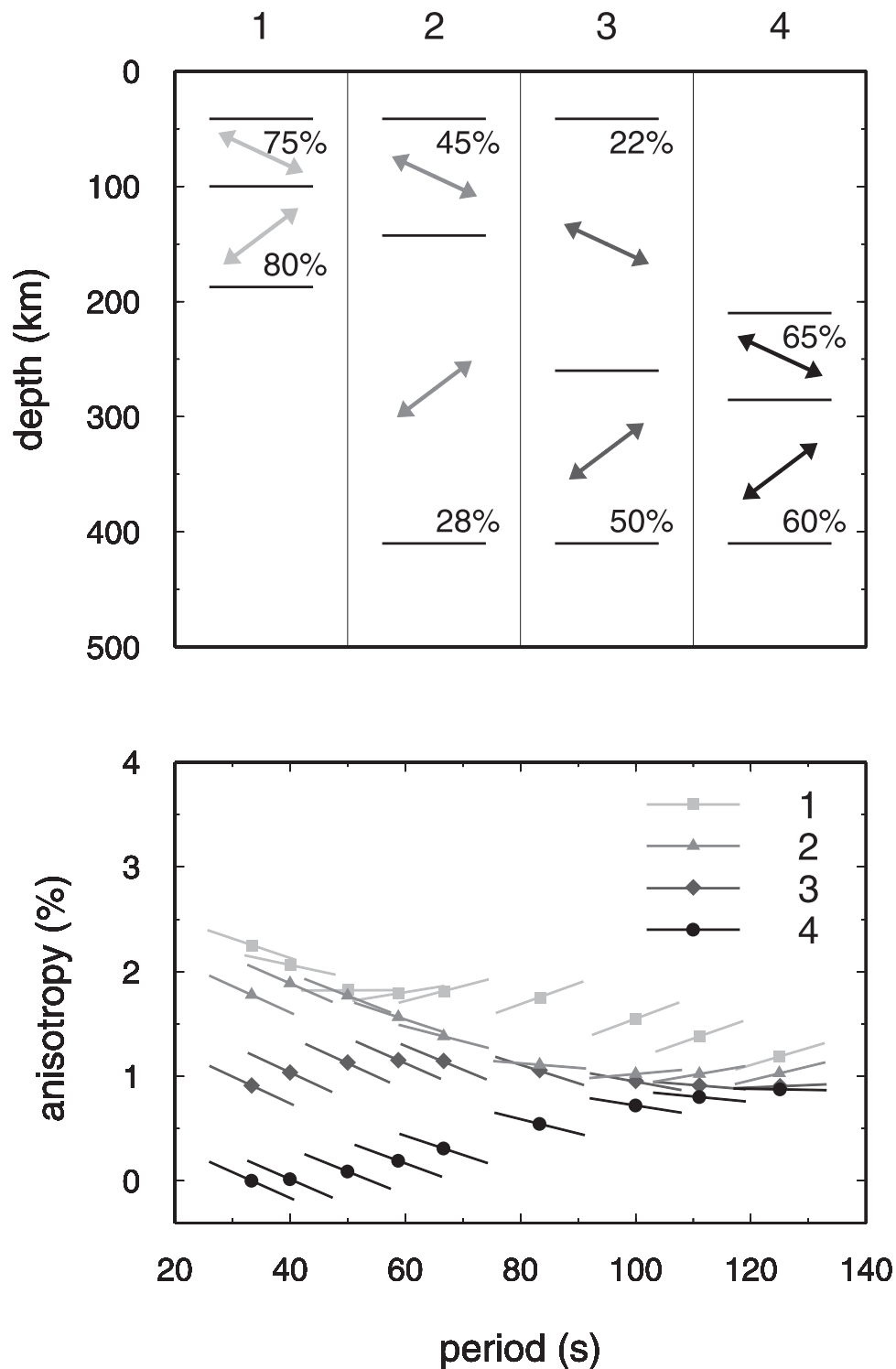


**Figure 16.** Two-layer anisotropic models and predicted azimuthal anisotropy. Fast directions in the top and bottom layers [Levin *et al.* 1999] are shown by arrows in the first panel from a map view. Layer thickness is indicated by two horizontal lines. The number in each layer indicates the percentage alignment of fast axes of olivine and orthopyroxene. The second panel shows the amplitude and fast direction of predicted anisotropy for each of the four models.

[59] (1) Crustal thickness varies from  $\sim 35$  km along the Atlantic coast to 45–50 km in the western Appalachians and in the portion of the Grenville Province in western New York. Crustal  $S$  wave velocity is generally 2.1–2.7% faster than

that in the global model AK135 with a standard deviation of  $\pm 0.5\%$ , and particularly high-velocity crust is observed beneath the Adirondack Mountains. The variation of crustal thickness correlates well with the observed Bouguer gravity

anomalies, and the travel time differences between  $P$  and  $S$  waves in the crust from our model are largely consistent with those from receiver function studies [Li et al., 2002a].

[60] (2) In the upper mantle, a high-velocity anomaly, which we interpret as the North America lithospheric keel, appears in the western part of the study area. The base of the keel has irregular morphology and could extend to 200 km or deeper, but our best estimates based on the depth to the maximum negative velocity gradient is that the base of the keel lies in the 100–150 km range. Thin lithosphere over low-velocity mantle is imaged from northern Connecticut to central Vermont and New Hampshire, and may be caused by thermal erosion of the lithosphere associated with the Monterey hot spot.

[61] (3) Azimuthal anisotropy from Rayleigh wave phase velocities was obtained assuming that anisotropy is uniform over the study area or varies between two subregions. The amplitude of the anisotropy is small, less than 1%, and unresolvably different from zero at periods less than 100 s. Comparison with the predicted anisotropy from velocity models constrained by shear wave splitting suggests that anisotropy cannot exist solely in the lithosphere and that much of the source of the shear wave splitting must lie deeper than 200 km.

[62] **Acknowledgments.** We would like to thank Michael Bostock, Vadim Levin, and Madeleine Zirbes for help in seismic data collection. We also thank Suzan van der Lee, Harley Benz, and Steve Roecker for information about instrument responses. Colin Thomson kindly provided us with his code for calculating phase velocities from layered anisotropic media. Constructive comments from Suzan van der Lee and Norm Sleep helped us to improve this paper. We thank Matt J. Fouch for providing shear wave splitting data and Daniel Scheirer for assistance in extracting gravity data. Figures were created using the GMT graphic package [Wessel and Smith, 1998]. This work was supported under National Science Foundation awards EAR-9614705 and EAR-9903026.

## References

- Alsina, D., R. Snieder, and V. Maupin, A test of the great circle approximation in the analysis of surface waves, *Geophys. Res. Lett.*, **20**, 915–918, 1993.
- Alsina, D., R. L. Woodward, and R. K. Snieder, Shear-wave velocity structure in North America from large-scale waveform inversion of surface waves, *J. Geophys. Res.*, **101**, 15,969–15,986, 1996.
- Babuska, V., and M. Cara, *Seismic Anisotropy in the Earth*, Kluwer Acad., Norwell, Mass., 1991.
- Barruol, G., P. G. Silver, and A. Vauchez, Seismic anisotropy in the eastern United States: Deep structure of a complex plate, *J. Geophys. Res.*, **102**, 8329–8348, 1997.
- Braile, L. W., W. J. Hinze, R. R. B. von Frese, and G. Randy Keller, Seismic properties of the crust and uppermost mantle of the conterminous United States and adjacent Canada, *Mem. Geol. Soc. Am.*, **172**, 655–680, 1989.
- Capon, J., Analysis of Rayleigh-wave multipath propagation at LASA, *Bull. Seismol. Soc. Am.*, **60**, 1701–1731, 1971.
- Clifford, A. A., *Multivariate Error Analysis*, John Wiley, Hoboken, N. J., 1973.
- Constable, S. C., R. L. Parker, and C. G. Constable, Occam's inversion: A practical algorithm for generating smooth models from electromagnetic sounding data, *Geophysics*, **52**, 279–288, 1987.
- Crough, S. T., Mesozoic hotspot epeirogeny in eastern North America, *Geology*, **9**, 2–6, 1981.
- Debayle, E., and B. L. N. Kennett, Anisotropy in the Australasian upper mantle from Love and Rayleigh waveform inversion, *Earth Planet. Sci. Lett.*, **184**, 339–351, 2000.
- Fischer, K. M., M. E. Wysession, T. J. Clarke, M. J. Fouch, G. I. Al-eqabi, P. J. Shore, R. W. Valenzuela, A. Li, and J. M. Zaslav, The 1995–1996 Missouri to Massachusetts broadband seismometer deployment, *IRIS News.*, **15**, 6–9, 1996.
- Forsyth, D. W., and A. Li, Array analysis of two-dimensional variations in surface wave velocity and azimuthal anisotropy in the presence of multipathing interference, in *Geophysical Monograph Series*, AGU, Washington, D.C., in press, 2003.
- Forsyth, D. W., S. Webb, L. Dorman, and Y. Shen, Phase velocities of Rayleigh waves in the MELT experiment on the East Pacific Rise, *Science*, **280**, 1235–1238, 1998.
- Fouch, M. J., K. M. Fischer, E. M. Parmentier, M. E. Wysession, and T. J. Clarke, Shear-wave splitting, continental keels, and patterns of mantle flow, *J. Geophys. Res.*, **105**, 6255–6275, 2000.
- Friederich, W., and E. Wielandt, Interpretation of seismic surface waves in regional networks: Joint estimation of wavefield geometry and local phase velocity—Method and tests, *Geophys. J. Int.*, **120**, 731–744, 1995.
- Friederich, W., E. Wielandt, and S. Stange, Non-plane geometries of seismic surface wavefields and their implications for regional surface-wave tomography, *Geophys. J. Int.*, **119**, 931–948, 1994.
- Grand, S. P., Mantle shear structure beneath the Americas and surrounding oceans, *J. Geophys. Res.*, **99**, 11,591–11,621, 1994.
- Grand, S. P., R. D. van der Hilst, and S. Widiyantoro, Global seismic tomography: A snapshot of convection in the earth, *GSA Today*, **7**, 1–7, 1997.
- Hatcher, R. D., Jr., Tectonic synthesis of the U.S. Appalachians, in *The Geology of North America*, vol. F-2, *The Appalachian-Ouachita Orogen in the United States*, edited by R. D. Hatcher Jr., W. A. Thomas, and G. W. Viele, pp. 511–535, Geol. Soc. of Am., Boulder, Colo., 1989.
- Heaman, L. M., and B. A. Kjarsgaard, Timing of eastern North American kimberlite magmatism: Continental extension of the Great Meteor hot-spot track, *Earth Planet. Sci. Lett.*, **178**, 253–268, 2000.
- Hittelman, A. M., J. O. Kinsfather, and H. Meyers, Geophysics of North America [CD-ROM], Natl. Geophys. Data Cent., Boulder, Colo., 1990.
- Hoffman, P. F., Precambrian geology and tectonic history of North America, in *The Geology of North America*, vol. A, *Overview*, edited by A. W. Bally and A. R. Palmer, pp. 447–512, Geol. Soc. of Am., Boulder, Colo., 1989.
- Hughes, S., and J. H. Luetgert, Crustal structure of the western New England Appalachians and the Adirondack Mountains, *J. Geophys. Res.*, **96**, 16,471–16,494, 1991.
- Hughes, S., and J. H. Luetgert, Crustal structure of the southeastern Grenville Province, northern New York state and eastern Ontario, *J. Geophys. Res.*, **97**, 17,455–17,479, 1992.
- Jordan, T. H., Composition and development of the continental tectosphere, *Nature*, **274**, 544–548, 1978.
- Kennett, B. L. N., E. R. Engdahl, and R. Buland, Constraints on seismic velocities in the Earth from travel times, *Geophys. J. Int.*, **122**, 108–124, 1995.
- King, S. D., and J. Ritsema, African hot spot volcanism: Small-scale convection in the upper mantle beneath cratons, *Science*, **290**, 1137–1140, 2000.
- Knopoff, L., Observation and inversion of surface-wave dispersion, *Tectonophysics*, **13**, 497–519, 1972.
- Larson, E. W. F., and G. Ekstrom, Global models of surface wave group velocity, *Pure Appl. Geophys.*, **158**(7), 1377–1400, 2001.
- Levin, V., W.-Y. Kim, and W. Menke, Seismic velocities in the shallow crust of western New England and northern New York, *Bull. Seismol. Soc. Am.*, **85**, 207–219, 1995.
- Levin, V., W. Menke, and A. Lerner-Lam, Seismic anisotropy in the northeastern U.S. as a source of significant teleseismic  $P$  travel time anomalies, *Geophys. J. Int.*, **126**, 593–603, 1996.
- Levin, V., W. Menke, and J. Park, Shear-wave splitting in the Appalachians and the Urals: A case for multilayered anisotropy, *J. Geophys. Res.*, **104**, 17,975–17,993, 1999.
- Levin, V., W. Menke, and J. Park, No regional anisotropic domains in the northeastern U. S. *Appalachians*, *J. Geophys. Res.*, **105**, 19,029–19,042, 2000.
- Li, A., K. M. Fischer, S. van der Lee, and M. E. Wysession, Crust and upper mantle discontinuity structure beneath eastern North America, *J. Geophys. Res.*, **107**(B5), 2100, doi:10.1029/2001JB000190, 2002a.
- Li, A., D. W. Forsyth, and K. M. Fischer, Evidence for shallow isostatic compensation of the southern Rocky Mountains from Rayleigh wave tomography, *Geology*, **30**, 683–686, 2002b.
- Li, A., et al., Rayleigh wave constraints on shear wave structure and azimuthal anisotropy beneath the Colorado Rocky Mountains, in *Geophysical Monograph Series*, AGU, Washington, D. C., in press, 2003.
- Martin, B. E., and C. J. Thomson, Modeling surface waves in anisotropic structures, part II, Examples, *Phys. Earth Planet. Inter.*, **103**, 253–279, 1997.
- Menke, W., and V. Levin, Anomalous seaward dip of the lithosphere-asthenosphere boundary beneath the northeastern U. S. detected using differential-array measurements of Rayleigh waves, *Geophys. J. Int.*, **149**, 413–421, 2002.

- Mitchell, B. J., Anelastic structure and evolution of the continental crust and upper mantle from seismic surface wave attenuation, *Rev. Geophys.*, *33*, 441–462, 1995.
- Montagner, J.-P., Regional three-dimensional structures using long-period surface waves, *Ann. Geophys. Ser. B*, *4*(3), 283–294, 1985.
- Montagner, J.-P., and D.-A. Griot-Pommeroy, How to relate body wave and surface wave anisotropy, *J. Geophys. Res.*, *105*, 9015–9027, 2000.
- Mooney, W. D., and L. W. Braile, The seismic structure of the continental crust and upper mantle of North America, in *The Geology of North America*, vol. A, *Overview*, edited by A. W. Bally and A. R. Palmer, pp. 39–52, Geol. Soc. of Am., Boulder, Colo., 1989.
- Morgan, W. J., Hotspot tracks and the early rifting of the Atlantic, *Tectonophysics*, *94*, 123–139, 1983.
- Musacchio, G., W. D. Mooney, J. H. Luetgert, and N. I. Christensen, Composition of the crust in the Grenville and Appalachian provinces of North America inferred from  $V_p/V_s$  ratios, *J. Geophys. Res.*, *102*, 15,225–15,241, 1997.
- Nataf, H. C., and Y. Ricard, 3SMAC: An a priori tomographic model of the upper mantle based on geophysical modeling, *Phys. Earth Planet. Inter.*, *95*, 101–102, 1996.
- Park, J., and V. Levin, Seismic anisotropy: Tracing plate dynamics in the mantle, *Science*, *296*, 485–489, 2002.
- Pearson, N. J., S. Y. O'Reilly, and W. L. Griffin, The crust-mantle boundary beneath cratons and craton margins: A transect across the southwest margin of the Kaapvaal craton, *Lithos*, *36*, 257–288, 1995.
- Press, W. H., S. A. Teukolsky, W. T. Vetterling, and B. P. Flannery, *Numerical Recipes in FORTRAN: The Art of Scientific Computing*, 2nd ed., 963 pp., Cambridge Univ. Press, New York, 1992.
- Rankin, D. W., Continental margin of the eastern United States: Past and present, in *Phanerozoic Evolution of North America Continent-Ocean Transitions*, edited by R. C. Speed, pp. 129–218, Geol. Soc. of Am., Boulder, Colo., 1994.
- Rondenay, S., M. G. Bostock, T. M. Hearn, D. J. White, and R. M. Ellis, Lithospheric assembly and modification of the SE Canadian Shield: Abitibi-Grenville teleseismic experiment, *J. Geophys. Res.*, *105*, 13,735–13,754, 2000.
- Shumaker, R. C., and T. H. Wilson, Basement structure of the Appalachian foreland in west Virginia: Its style and effect on sedimentation, in *Basement and Basins of Eastern North America*, edited by B. A. van der Pluijm and P. A. Catacosinos, *Geol. Soc. Am. Spec. Pap.* *308*, pp. 139–168, Geol. Soc. of Am., Boulder, Colo., 1996.
- Silver, P. G., Seismic anisotropy beneath the continents: Probing the depth of geology, *Annu. Rev. Earth Planet. Sci.*, *24*, 385–432, 1996.
- Simons, F. J., R. D. van der Hilst, J.-P. Montagner, and A. Zielhuis, Multimode Rayleigh wave inversion for heterogeneity and azimuthal anisotropy of the Australian upper mantle, *Geophys. J. Int.*, *151*, 738–754, 2002.
- Sleep, N. H., Monteregean hotspot track: A long-lived mantle plume, *J. Geophys. Res.*, *95*, 21,983–21,990, 1990.
- Smith, M. L., and F. A. Dahlen, The azimuthal dependence of Love and Rayleigh wave propagation in a slightly anisotropic medium, *J. Geophys. Res.*, *78*, 3321–3333, 1973.
- Tarantola, A., and B. Valette, Generalized non-linear problems solved using the least-squares criterion, *Rev. Geophys.*, *20*, 219–232, 1982.
- Taylor, S. R., Geophysical framework of the Appalachians and adjacent Grenville province, *Mem. Geol. Soc. Am.*, *172*, 317–348, 1989.
- Thomson, C. J., Modeling surface waves in anisotropic structures, part I, Theory, *Phys. Earth Planet. Inter.*, *103*, 195–206, 1997.
- vanDecar, J. C., D. E. James, and M. Assumpcao, Seismic evidence for a fossil mantle plume beneath South America and implications for plate driving forces, *Nature*, *378*, 25–31, 1995.
- Van der Lee, S., High-resolution estimates of lithospheric thickness from Missouri to Massachusetts, USA, *Earth Planet. Sci. Lett.*, *203*, 15–23, 2002.
- Van der Lee, S., and G. Nolet, Upper mantle S-velocity structure of North America, *J. Geophys. Res.*, *102*, 22,815–22,838, 1997.
- Vinnik, L. P., L. I. Makeyeva, A. Milev, and A. Y. Usenko, Global patterns of azimuthal anisotropy and deformation in the continental mantle, *Geophys. J. Int.*, *111*, 433–447, 1992.
- Wessel, P., and W. H. F. Smith, New improved version of the Generic Mapping Tools released, *Eos Trans. AGU*, *79*(47), 579, 1998.
- Wolfe, C. J., and S. C. Solomon, Shear-wave splitting and implications for mantle flow beneath the MELT region of the East Pacific Rise, *Science*, *280*, 1230–1232, 1998.
- Zhu, H., and J. E. Ebel, Tomographic inversion for the seismic velocity structure beneath northern New England using seismic refraction data, *J. Geophys. Res.*, *99*, 15,331–15,358, 1994.

---

K. M. Fischer and D. W. Forsyth, Department of Geological Sciences, Brown University, Providence, RI 02912, USA. (karen\_fischer@brown.edu; donald\_forsyth@brown.edu)

A. Li, Department of Geosciences, University of Houston, Science and Research Bldg. 1, Houston, TX 77204, USA. (ali2@mail.uh.edu)